Intensity of the Earth's magnetic field: evidence for a Mid-Paleozoic dipole low

Louise M. A. Hawkins[1], Joseph Grappone[1], Courtney Sprain[2], Patipan Saengduean[3], Edward Sage[4], Sheikerra Thomas-Cunningham[1], Banusha Kugabalan[5], and Andrew Biggin[1]

[1]University of Liverpool
[2]University of Floria
[3]Colorado School of Mines
[4]CGG Satellite Mapping
[5]University of Glasgow

November 24, 2022

Abstract

The Mesozoic Dipole Low (MDL) is a period, covering at least ˜80 million years, of low dipole moment that ended at the start of the Cretaceous Normal Superchron. Recent studies of Devonian age Siberian localities identified similarly low field values a few tens of million years prior to the Permo-Carboniferous Reverse Superchron (PCRS). To constrain the length and timing of this potential new dipole low, this study presents new paleointensity estimates from Strathmore (˜411-416 Ma) and Kinghorn (˜332 Ma) lava flows, UK. Both localities have been studied for paleomagnetic poles (Q values of 6-7) and the sites were assessed for their suitability for paleointensity from paleodirections, rock magnetic analysis, and microscopy. Thermal- and microwave-IZZI protocol experiments were used to determine site mean paleointensity estimates of ˜3-51 μT (6-98 ZAm^2) and 4-11 μT (9-27 ZAm^2) from the Strathmore and Kinghorn localities, respectively. These, and all of the sites from 200-500 Ma from the (updated) PINT15 database, were assessed using the Qualitative Paleointensity criteria (Q?I). The procurement of reliable (Q?I [?]5), weak paleointensity estimates from this and other studies indicates a period of low dipole moment (median field strength of 17 ZAm^2) for ˜80 Myrs, from 332-416 Ma. This "Mid-Paleozoic Dipole Low (MPDL)" bears a number of similarities to the MDL, including the substantial increase in field strength near the onset of the PCRS. The MPDL also adds support to inverse relationship between reversal frequency and field strength and a possible ˜200 million-year cycle in paleomagnetic behavior relating to mantle convection.

Intensity of the Earth's magnetic field: evidence for a Mid-Paleozoic dipole low

Louise M. A. Hawkins[1]*, J. Michael Grappone[1], Courtney J. Sprain[1,2], Patipan Saengduean[1,*3], Edward J. Sage[1,*4], Sheikerra Thomas-Cunningham[1], Banusha Kugabalan[1,*5], Andrew J. Biggin[1]

[1]*Geomagnetism Laboratory, Department of Earth, Ocean and Ecological Sciences, University of Liverpool, Liverpool L69 7ZE, United Kingdom*

[2]*Department of Geological Sciences, The University of Florida, 241 Williamson Hall, PO Box 112120, Gainesville, FL, United States*

[*3]*Department of Geophysics, Colorado School of Mines, 1500 Illinois St., Golden, CO 80401, United States*

[*4]*CGG Satellite Mapping, Crockham Park, Edenbridge, Kent, TN8 6SR, United Kingdom*

[*5]*School of Physics & Astronomy, Kelvin Building, University of Glasgow, Glasgow, G12 8QQ, Scotland, United Kingdom*

Abstract

The Mesozoic Dipole Low (MDL) is a period, covering at least ~80 million years, of low dipole moment that ended at the start of the Cretaceous Normal Superchron. Recent studies of Devonian age Siberian localities identified similarly low field values a few tens of million years prior to the Permo-Carboniferous Reverse Superchron (PCRS). To constrain the length and timing of this potential new dipole low, this study presents new paleointensity estimates from Strathmore (~411-416 Ma) and Kinghorn (~332 Ma) lava flows, UK. Both localities have been studied for paleomagnetic poles (Q values of 6-7) and the sites were assessed for their suitability for paleointensity from paleodirections, rock magnetic analysis, and microscopy. Thermal- and microwave-IZZI protocol experiments were used to determine site mean paleointensity estimates of ~3-51 µT (6-98 ZAm^2) and 4-11 µT (9-27 ZAm^2) from the Strathmore and Kinghorn localities, respectively. These, and all of the sites from 200-500 Ma from the (updated) PINT15 database, were assessed using the Qualitative Paleointensity criteria (Q_{PI}). The procurement of reliable (Q_{PI} ≥5), weak paleointensity estimates from this and other studies indicates a period of low dipole moment (median field strength of 17 ZAm^2) for ~80 Myrs, from 332-416 Ma. This "Mid-Paleozoic Dipole Low (MPDL)" bears a number of similarities to the MDL, including the substantial increase in field strength near the onset of the PCRS. The MPDL also adds support to inverse relationship between reversal frequency and field strength and a possible ~200 million-year cycle in paleomagnetic behavior relating to mantle convection.

Significance Statement

Variations in past geomagnetic field strength are an important indicator of variation in deep-Earth processes over hundreds of millions of years because very little other information is preserved. New measurements from northern UK, in addition to the existing datasets, show the field was weak for tens of millions of years between 332-416 Ma. The similarities between this and a later period of low field strength provide further evidence to both a potential ~200 million-year cycle lined to deep Earth processes.

Introduction

The evolution of the Earth's deep interior, although critical to our understanding of the planet's history, is inadequately defined due to poor preservation of materials that formed deep within the Earth and that most geophysical techniques can only constrain geologically recent deep Earth processes. Comparatively, the paleomagnetic record, and paleointensity in particular, has served as a key indicator of early deep Earth processes, such as the initiation of the geodynamo (1) and inner core nucleation (e.g. 2, 3). During the Phanerozoic, superchrons (periods of tens of millions of years without magnetic polarity reversals) are suggested to be linked to changes in Earth's deep interior. Three superchrons have been identified (4) and correspond with peaks in field strength (5). The superchrons alternate with suspected periods of frequently-reversing weak dipole moments. If confirmed, this pattern would suggest the existence of a ~200 million-year (Myr) cycle in paleomagnetic behavior, likely resulting from deep Earth processes (6), which alternates between superchrons and these periods of low magnetic dipole moments, such as the Mesozoic Dipole Low (MDL). First proposed by Prevot et al. (7), the MDL is a period of low dipole moment suggested to have lasted for at least the ~80 Myrs preceding the Cretaceous Normal Superchron (CNS: 84-126 Ma). The MDL has since been confirmed by subsequent studies (8, 9), potentially originating near the end of the Permo-Carboniferous (Kiaman) Reversed Superchron (PCRS; 267-315 Ma; 10). It has also been suggested that the MDL is actually confined to ~150-170 Ma, while the rest of the "MDL" is biased towards low field values due to rock magnetic effects (11). Recent research from Siberian sites (12, 13) found a similar persistent, low dipole strength magnetic field during the Devonian (359 – 419 Ma), lasting ~50 Myrs, ~35 Myrs prior to the start of the PCRS. However, it is still unclear if the behavior of the magnetic field during the Devonian and Early Carboniferous (~100 Myrs pre-PCRS) is comparable to that of the MDL, as there is very little available data, with only five studies from this age in the Palaeointensity Database (PINT15; 14).

To quantify the length of this potential dipole low, two localities from the east coast of Scotland, UK were selected from this time period to augment the previously published studies (Fig. 1). The first of these, lava flows from the Strathmore region (411-416 Ma; 13), were initially studied comprehensively by Sallomy and Piper (16), who found paleodirections consistent with this early Devonian age. A follow-up paleointensity study by Kono (17), based on a subset of these sites, gave a mean virtual dipole moment (VDM) of ~35 ZAm^2, which is substantially lower than the present-day field strength (~80 ZAm^2). However, the reliability of this study is unclear, as it was done prior to the development of modern day paleointensity techniques and selection criteria. No checks for alteration or multi-domain behavior were included, and studies have shown that the perpendicular protocol that was used can give artificially low paleointensities (18). The original paleodirectional study has also since been superseded by Torsvik (19). This updated study argued that the high degree of scatter and the presence of sites with 'transitional' directions in the original study, several of which were used for paleointensity, was likely due to bias introduced by the demagnetization techniques used and local tectonic effects.

The second locality, lava flows from the beaches along Kinghorn and Burntisland, Scotland (332 ± 5.6; 20), has not been studied for paleointensity previously. A paleodirectional study carried out on these lavas by Torsvik (21) found primary directions that were used to determine an Early Carboniferous pole. The new experimental results are presented herein alongside a detailed meta-analysis of published datasets dated to 200–500 Ma using paleointensity quality criteria

(Q_{PI}; 23). The outcome supports a new key feature of long-term geomagnetic behavior: the mid-Paleozoic dipole low (MPDL).

Materials and Methods

Detailed geological backgrounds of the Strathmore and Kinghorn localities, along with a description of the sampling techniques used, are provided in *Geological Background and Sampling (S1)* and the location of the sites sampled are shown in Fig. 1. The suitability of these sites for paleointensity analysis was first determined using paleodirectional and rock magnetic analysis. The majority of sites were initially stepwise thermally demagnetised (see *Methods: Paleodirections (S1)* for details) to determine if the samples carried a stable magnetic remanence. Selection criteria applied to the individual paleodirections obtained were an anchored, maximum angular deviation (MAD_{ANC} ≤10°) and the angle between the anchored and unanchored directions (α ≤10°). Additionally, site directions required some degree of clustering (k ≥15), before being compared with those from the previous studies (19, 21) to determine if the magnetization was of the correct age. Rock magnetic analysis was also performed on all sites, including hysteresis, isothermal remanent magnetization (IRM), back-field and thermomagnetic (Curie) measurements (see *Methods: Rock Magnetics (S1)* for details). These measurements, in conjunction with scanning electron microscopy (SEM) analysis, were used to determine if the remanence carriers were consistent with the sites carrying a primary Thermal Remanent Magnetization (TRM). Sites that passed all the criteria were then used for paleointensity analysis. Both microwave and thermal Thellier-type paleointensity experiments were performed using the IZZI protocol (23) with partial TRM (pTRM) checks (24). Full details of the experimental procedure used, including selection criteria applied, is provided in *Methods: Paleointensity (S1)*.

Results

A detailed outline of the results of the paleodirectional and rock magnetic analysis carried out on these two localities is described under *Results* (S1). Of the twelve Strathmore sites that gave acceptable paleodirections, seven were determined to be suitable for paleointensity experimentation. In turn, two of these sites were combined into a single site (WB1/2) as the directions show that the baked sediment (WB1) acquired its TRM at the same time as the overlying lava (WB2). All the Kinghorn sites that passed the paleodirection selection criteria (six out of nine sites) were deemed suitable for paleointensity, along with two additional sites (KHA-B; Fig. S1b). All these sites produced reversible thermomagnetic curves below their Curie temperature (T_C), indicating specimens did not alter substantially when heated. From the Strathmore dataset, a few sites (CB1, SN1, WB1) produced thermomagnetic curves that indicated the presence of two magnetic minerals, magnetite and hematite (Fig S2a). The igneous sites with both remanence carriers (CB1 and SN1) may hold primary remanences because the paleodirectional component is from a temperature range that potentially spans both minerals (340-680 °C), while WB1 is a baked sediment whose directions are consistent with the overlying lava (WB2). The rest of the studied Strathmore and Kinghorn sites all had single Tc's; some of those from the Kinghorn sites were consistent with relatively Ti-rich titanomagnetite. (KH1, A-B; Fig. S2d), while the rest from both localities (WB2-5, KH2,4,7-10) were consistent with magnetite or low-Ti titanomagnetite (Fig. S2b, c). SEM work completed on representative specimens from magnetite- and titanomagnetite-bearing sites show primary igneous textures (i.e. coarse exsolution structures) and no evidence of low temperature oxidation (Fig. S2e, f). The majority of these sites have hysteresis parameters that fall between those expected for single-domain (SD) and multi-domain (MD) magnetic remanence carriers (Fig S2g, h) and fall near but above the bulk domain stability trendline (25).

From the Strathmore locality, 35 out of 82 paleointensity measurements passed selection criteria (given in Table S1; pass rate of 43%) across the six sites. All but one site gave low site-mean paleointensity estimates (3.1-19.7 μT), corresponding to VDMs between 5.6 and 46.2 ZAm^2 (Table 1), while site CB1 gave a singularly high site mean estimate of 50.9 μT (98.0 ZAm^2). The majority of accepted Strathmore estimates are from thermal experiments because the microwave demagnetization mechanism was largely unsuitable for hematite bearing sites (CB1, SN1, WB1). The other estimates were split approximately evenly between the two techniques. The pass rate for microwave experiments was 48% vs. 36% for thermal results for the sites that had both. Example Arai plots (Fig. 2) show the range of behaviour exhibited from the six sites and the different techniques used. The hematite-bearing sites (Fig. 1a, b) showed minimal demagnetization at temperatures below 300°C and linear Arai plots across the temperature ranges for magnetite or both magnetite and hematite. From Wormit Bay, sites WB2 and WB3 behave similarly, as do WB4 and WB5, likely because of the similarities in grain size, based on the hysteresis properties of the sites (Fig S2g). Sites WB2-3 lie close to the MD range but produce near-linear orthogonal vector and Arai plots, whereas sites WB4-5 exhibit some zig-zagging of the corresponding orthogonal plots and the only occurrence of two-sloped Arai plots. In these cases, however, a visible change in direction is associated with the two components (although the change is not substantial because Devonian age directions are often close to present day directions e.g. 11).

Of the Kinghorn locality samples, 53 out of 143 measurements passed selection criteria (given in Table S2; pass rate of 37%). All sites produced very low site mean estimates (3.7-10.9 μT; Table 1), corresponding to exceptionally low VDM estimates (9.6-27.0 ZAm^2). The majority of the accepted measurements were made using the microwave system, as it had a much higher success rate (54% success rate vs. the 9% success rate for thermal experiments). This may be because the relatively Ti-rich titanomagnetite is prone to altering more in the thermal than microwave experiments due to reduced bulk heating of the samples in the latter (26). The appearance of the Arai plots varies, with some sites producing near linear plots with minimal overprints (Fig. 2a, f), whereas others exhibit varying degrees of two-slope behaviour (Fig 2b-e). Like sites WB4-5 described above, the two-slope Arai plots all show a corresponding slight change in direction, which suggests the steep, low-temperature slope is likely an overprint rather than due to non-ideal behaviour. There is no clear correlation between the appearance of the Arai plots and either the titanium content of the titanomagnetite or the apparent grain size (Fig. S2h).

Discussion

Reliability of 200-500 Ma sites

To further assess the reliability of these new site-mean, paleointensity estimates, and to provide a framework for comparing them to others from the Paleozoic (~252-541 Ma), all the sites were evaluated using Q_{PI} criteria. Biggin and Paterson (27) proposed these nine criteria to acknowledge and mitigate the potential biases that affect the interpretation of paleointensity data and are applied in a similar way to Q criteria for paleomagnetic poles (28). Sites that have published information addressing a criterion pass (score a 1), and, if not, they fail (score a 0). The Q_{PI} score for the site is the sum of the individual criterion scores. A detailed explanation of the how the

Kinghorn and Strathmore sites were scored is provided in *Results: Q_{PI} scoring (S1)*, while a summary of the scores is provided in Table 1. The new Strathmore sites in this study received Q_{PI} scores ranging from 5 to 8 (median: 6.5, mean: 6.3), out of a possible 9. The new Kinghorn sites similarly received Q_{PI} scores ranging from 6 to 8 (with a slightly higher median of 7 and mean of 6.8). STAT and LITH are the Q_{PI} criteria that the majority of sites failed. The failure to meet STAT is largely because the sites gave low palaeointensity estimates, which are less likely to pass STAT due to how it is defined, and LITH because only one site had a suitable contact lithology that could be sampled. MD and TRM failing for some of the Strathmore sites is why its Q_{PI} scores are slightly lower than those of the Kinghorn sites, although the results are considered reliable as the sites still scored highly and are very similar to those from Russia of a similar age (7-39 ZAm^2 with a single outlier site of 98 ZAm^2; 10).

Integration of these new estimates with an existing Paleozoic dataset first requires determination of what published data are sufficiently robust for meta-analysis. All the data in the PINT15 database (12) from 200-500 Ma were checked against their corresponding study to fix any errors. Ages were recalculated where possible (e.g. stratigraphic ages were revised to be consistent with the most recent timescale (ICS2020/v1), isotopic ages were replaced where superseding ages are known, etc.). The biggest reassessment of site ages comes from the apparently Middle-Late Carboniferous from Uzbekistan (29, 30).The relative ages between sites and the single inclination sign across multiple sections, with 13-40 sites per section, indicate that these sites could only come from the part of the Carboniferous during the PCRS (i.e. Moscovian-Gzhelian; 298.9-315.2 Ma). Sites from 5 studies published since the last PINT15 update were also added (references listed in Dataset S4). Q_{PI} criteria were applied to all the sites, based on the published information from the corresponding studies. This time period covers both the PCRS and the surrounding time periods, which allows paleomagnetic field strengths during the superchron to be compared with those from a reversing field. This time period also complements two other Q_{PI} studies that assessed the PINT15 database for 500-3500 Ma (2) and 65-200 Ma (11).

The revised PINT15 data for 200-500 Ma, including Q_{PI} scoring, is included in Dataset S3. A workflow for the scores provided is outlined in Dataset S4, and the age distribution, coverage, and reliability of the revised 200-500 Ma PINT15 data is illustrated in Fig. 4. Given that most studies from this time period were published before Q_{PI} criteria existed, their Q_{PI} scores tend to be lower because there is insufficient information published to confirm that a potential issue has been addressed, rather than it being clear that that issue has affected the estimates. Only sites with Q_{PI} scores of 0 will be excluded entirely; these either have no published information to support the reliability of the site means or they have been confirmed to be unreliable. All the highest scoring sites (Q_{PI} ≥5) are found in the time periods immediately before (16 sites) and after (26 sites) the PCRS, which comprises the data from this study along with recently published studies (12, 13). While there are numerous sites with PCRS ages, 144 of the 195 sites (74%) covering this period come from just four studies: (29, 31–33). The Q_{PI} scores for these are low because these publications use outdated paleointensity methods and include very little supporting information.

Paleozoic Field Variation

Based on the pattern of field strength variation from these new site means and the existing PINT15 dataset, weighted by Q_{PI} score (Fig.4), a relatively long period of low dipole moment presents itself in the period preceding the PCRS, followed by a substantial increase in field strength during the superchron relative to periods of reversing field. To evaluate whether this variation is similar to that observed during the Mesozoic, analysis was performed, following the methodology of previous studies (2, 11), by comparing the field strength distribution of different periods, filtered by Q_{PI} scoring. The combined dataset was grouped into 3 bins using the superchron as an anchor: PRE (315-416 Ma), PCRS (267-315 Ma), and POST (200-267 Ma). Fig.5 illustrates the distribution of site VDMs in these bins, for different Q_{PI} minima, while details of the data included in these bins are included in Table S2. Kulakov et al. (11) was able to identify periods of distinct dipole moment during the MDL based on reversal frequency. However, the reversal record prior to the PCRS is too sparse to apply the same technique (Fig. 4), so the PRE bin was not divided further. Its maximum age bound was set to 416 Ma to avoid the Ordovician Reversed Superchron (ORS; 461-480 Ma; 34) and because there are no estimates with $Q_{PI} \geq 1$ between 416-461 Ma. There is no analysis of the ORS, or the period before it, as between 461-500 Ma there are only 3 available estimates. The age distribution of the POST bin is also substantially skewed (skewness = -6.14 at $Q_{PI} \geq 3$; see Table S2) as there are only 13 site-mean results between 200-250 Ma and an abundance of data around ~250 Ma. This peak in the data is almost entirely the result of a large number of studies from the Siberian Traps (see Anwar (10) for details); however, the paucity of data between 200-250 Ma means it cannot be connected to the Early bin from Kulakov et al. (11) and should be considered independent of it.

A minimum acceptable cut-off of $Q_{PI} \geq 3$ has previously been applied to reduce misfits while still maintaining sufficient data (2, 11) and is similarly implemented here. It is clear from Fig. 5, however, that the dipole moment during the PCRS is substantially higher than the surrounding time periods, regardless of Q_{PI} filtering. The bin medians also do not change substantially until $Q_{PI} \geq 4$ (Fig. 4), and Kolomogorv-Smirnov (K-S) tests comparing the bins pair-wise reject the null hypothesis that the datasets come from the same distribution at the 1% significance level up to $Q_{PI} \geq 5$ (Table S2). In both these cases, the changes likely result from the number of estimates in the bins, particularly the PCRS and POST bins, being too small to be significant above this level. At $Q_{PI} \geq 3$, the median field during the PCRS is 80 ZAm^2, while the PRE and POST bins are 17 ZAm^2 and 23.6 ZAm^2 respectively. The PCRS median is much higher than that of the CNS at $Q_{PI} \geq 3$ (48 ZAm^2; 37) , which brings into question the reliability of the average strength of the field during the PCRS. However, the mean PCRS value (76 ZAm^2) is around the proposed mean for the CNS (80 ZAm^2; 5), and the difference appears to be that there are more low estimates recorded for the CNS than the PCRS. This is probably due to the greater number of, and more recent, studies available for the CNS and explains why the PCRS median drops to a similar value to that of the CNS at $Q_{PI} \geq 4$, as the 4 studies that make up the bulk of the PCRS have Q_{PI} scores ≤3. While the difference in average field strength between the PCRS and the rest of the Paleozoic is likely to remain, further studies may be needed to evaluate if the variation between the average field strength during the two superchron is valid or due to data bias.

The median values for the PRE and POST bins are very low and closest to that of the the Jurassic Hyperactivity period (JHAP; 155-171 Ma; 26 ZAm^2 for all data points as there is insuffcent data at $Q_{PI} \geq 3$; 35) which had an average reversal frequency of ~11 Myr^{-1}. In comparison, the other periods of reversing field during the Mesozoic (Early, Mid, Late; 11) had median field strengths of 36-48 ZAm^2, with reversal frequencies of 1-3 Myr^{-1}. The low average field strength of the POST bin, along with the VDM distribution appearing distinct from the PRE bin based on K-S testing, is probably due to under-sampling average field behavior during this time as the POST bin is almost exclusively from sites emplaced over ~800,000 years (the Siberian Trap sites;36). This should not be the case for the PRE bin; however, it is possible that the low average field strength may be partly due to recent studies (with higher Q_{PI} scores) tending to sample periods of very high reversal frequency similar to the JHAP. This is difficult to constrain because the magnetostratigraphic records before the PCRS are generally too sparse to provide a reliable record of reversal frequency. A recent magnetostratigraphic study from the Canning Basin (37) suggests reversal frequencies of a minimum of 2-5 Myr^{-1} around the same time that the Viluy sites cooled (~360 Ma; 12). In addition, an evaluation of reversal frequency ~8-14 Myrs before the PCRS (38) suggests reversal frequencies of ~12 Myr^{-1}, very similar to the high JHAP values, occurring ~5 Myr after the Kinghorn lavas (this study) erupted. These studies produced notably weak site mean values in the range of 4–27 ZAm^2. A greater non-dipole component to the field, relative to the present day, is also indicated for some of the Siberian sites, such as the Minusa (12) and the aforementioned Viluy Traps (13), although the new sites herein provide no indication of a greater non-dipole component, despite comparable timing and field strength estimates. A final consideration is that the average Phanerozoic geomagnetic field strength is significantly lower than the modern field, around 78 ZAm^2 (39), whereas the average for the Phanerozoic has been suggested to be around 42 ZAm^2 (8) or 50 ZAm^2 (2). Possible causes cited for this, such as MD effects on paleointensity experiments (40) and/or aging of TRM (41), may also explain why the MPDL appears weaker than the MDL as these problems are likely to be more pronounced as samples age.

A Mid-Paleozoic Dipole Low and its implications for deep mantle variation

Despite some potential biases of the dataset, as discussed in the previous sections, the evaluation of the period of low dipole moment leading up to the PCRS provided by this study suggests it is a significant and distinct feature of the Paleozoic paleomagnetic record (see K-S tests in Table S2). The proposed term for this feature, the mid-Paleozoic dipole low (MPDL), is based on its similarities to the MDL. These similarities include the weak field (discussed in previous section) and the ~80 Myrs duration, from ~416-332 Ma. In both cases, however, gaps in the record make it difficult to confirm if the period of low dipole moment extends back further in time (13). The average field strength has been shown to vary throughout the MDL (11), and there is also evidence for a difference (see Fig. 4) between the relatively strong early part between 390-416 Ma (median of 36 ZAm^2), based on the Minusa (42) and Strathmore (this study) sites, and the rest of the MPDL (317-390 Ma; median of 14 ZAm^2). Unlike the MDL, the low field strength is difficult to relate directly to reversal frequency due to the paucity of the magnetostratigraphic record at this time. Finally, there is a clear increase in field strength around the onset of the PCRS, potentially 3-4x the field strength of the pre-PCRS field if the average PCRS field strength is reliable, although a gap in the dataset exists from ~20 Myrs prior to the PCRS to an unknown point in the superchron (assumed to be within the Carboniferous part of the PCRS; 299-315 Ma). The large age uncertainties associated with the early PCRS sites prevent a clear determination of this transition.

The newly assessed paleointensity record provided in this study gives an improved indication of patterns in Phanerozoic paleomagnetic field behavior across 10–100 Myr timescales (6) back to ~415 Ma. The similarities observed herein between the MPDL and the MDL prior to their respective superchrons provide more evidence for the proposed inverse relationship between field strength and reversal frequency. There are insufficient paleointensity sites prior to (3 sites) and during (0 sites) the ORS to test this theory further back in time. There have been several mechanisms proposed for this variation in field behavior relating to mantle plumes (43, 44), subduction (45) and True Polar Wander (6), however, the extension of our reliable Phanerozoic paleointensity record now exceeds the length for the reliable portions of these records and so further work is needed to link the MPDL to any of these processes.

Acknowledgments

We would like to thank Elliot Hurst, Neil Suttie and Thomas Beckwith, who assisted in sample collection. LMH, CJS and AJB acknowledge funding NERC standard grant NE/P00170X/1. LMH further acknowledges funding from NERC Studentship 1511981. JMG acknowledges support from the NERC EAO Doctoral Training Partnership (grant NE/L002469/1), the Duncan Norman Research Scholarship, and NERC studentship 1793213.

References

1. J. A. Tarduno, R. D. Cottrell, W. J. Davis, F. Nimmo, R. K. Bono, A Hadean to Paleoarchean geodynamo recorded by single zircon crystals. *Science.* **349**, 521–524 (2015).
2. A. J. Biggin, *et al.*, Palaeomagnetic field intensity variations suggest Mesoproterozoic inner-core nucleation. *Nature* **526**, 245–248 (2015).
3. R. K. Bono, J. A. Tarduno, F. Nimmo, R. D. Cottrell, Young inner core inferred from Ediacaran ultra-low geomagnetic field intensity. *Nat. Geosci.* **12**, 143–147 (2019).
4. V. Pavlov, Y. Gallet, A third superchron during the Early Paleozoic. *Episodes* **28**, 78–84 (2005).
5. L. Tauxe, H. Staudigel, Strength of the geomagnetic field in the Cretaceous Normal Superchron: New data from submarine basaltic glass of the Troodos Ophiolite. *Geochemistry, Geophys. Geosystems* **5** (2004).
6. A. J. Biggin, *et al.*, Possible links between long-term geomagnetic variations and whole-mantle convection processes. *Nat. Geosci.* **5**, 526–533 (2012).
7. M. Prévot, M. E.-M. Derder, M. McWilliams, J. Thompson, Intensity of the Earth's magnetic field: Evidence for a Mesozoic dipole low. *Earth Planet. Sci. Lett.* **97**, 129–139 (1990).
8. L. Tauxe, J. S. Gee, M. B. Steiner, H. Staudigel, Paleointensity results from the Jurassic: New constraints from submarine basaltic glasses of ODP Site 801C. *Geochemistry, Geophys. Geosystems* **14** (2013).
9. D. N. Thomas, A. J. Biggin, Does the mesozoic dipole low really exist? *Eos Trans. AGU* **84**, 97–104 (2003).
10. T. Anwar, L. Hawkins, V. A. Kravchinsky, A. J. Biggin, V. E. Pavlov, Microwave paleointensities indicate a low paleomagnetic dipole moment at the Permo-Triassic boundary. *Phys. Earth Planet. Inter.* **260**, 62–73 (2016).
11. E. V Kulakov, *et al.*, Analysis of an updated paleointensity database (QPI-PINT) for 65-200 Ma: Implications for the long-term history of dipole moment through the Mesozoic. *J. Geophys. Res. Solid Earth* **124**, 9999–10022 (2019).
12. V. V. Shcherbakova, *et al.*, Was the Devonian geomagnetic field dipolar or multipolar? Palaeointensity studies of Devonian igneous rocks from the Minusa Basin (Siberia) and the Kola Peninsula dykes, Russia. *Geophys. J. Int.* **209**, 1265–1286 (2017).
13. L. M. A. Hawkins, *et al.*, An exceptionally weak Devonian geomagnetic field recorded by the Viluy Traps, Siberia. *Earth Planet. Sci. Lett.* **506**, 134–145 (2019).
14. A. J. Biggin, G. H. M. A. Strik, C. G. Langereis, The intensity of the geomagnetic field in the late-Archaean: New measurements and an analysis of the updated IAGA palaeointensity database. *Earth, Planets Sp.* **61**, 9–22 (2009).
15. M. F. Thirlwall, Geochronology of Late Caledonian magmatism in northern Britain. *J. Geol.*

Soc. London. **145**, 951–967 (1988).
16. J. T. Sallomy, J. D. A. Piper, Palaeomagnetic Studies in the British Caledonides - IV Lower Devonian Lavas of the Strathmore Region. *Geophys. Journal, R. Astron. Soc.* **34**, 47–68 (1973).
17. M. Kono, Palaeomagnetism and palaeointensity studies of Scottish Devonian volcanic rocks. *Geophys. J. Int.* **56**, 385–396 (1979).
18. J. M. Grappone, A. J. Biggin, M. J. Hill, Solving the mystery of the 1960 Hawaiian lava flow: implications for estimating Earth's magnetic field. *Geophys. J. Int.* **218**, 1796–1806 (2019).
19. T. H. Torsvik, Magnetic properties of the Lower Old Red Sandstone lavas in the Midland Valley, Scotland; palaeomagnetic and tectonic considerations. *Phys. Earth Planet. Inter.* **39**, 194–207 (1985).
20. S. Brindley, E. Spinner, Palynological assemblages from Lower Carboniferous deposits, Burntisland district, Fife, Scotland. *Proc. Yorksh. Geol. Soc.* **47**, 215–231 (1989).
21. T. H. Torsvik, O. Lyse, G. Atterás, B. J. Bluck, Palaeozoic palaeomagnetic results from Scotland and their bearing on the British apparent polar wander path. *Phys. Earth Planet. Inter.* **55**, 93–105 (1989).
22. A. J. Biggin, G. A. Paterson, A new set of qualitative reliability criteria to aid inferences on palaeomagnetic dipole moment variations through geological time. *Front. Earth Sci.* **2**, 1–9 (2014).
23. Y. Yu, L. Tauxe, Testing the IZZI protocol of geomagnetic field intensity determination. *Geochemistry, Geophys. Geosystems* **6** (2005).
24. R. S. Coe, S. Grommé, E. A. Mankinen, Geomagnetic paleointensities from radiocarbon-dated lava flows on Hawaii and the question of the Pacific nondipole low. *J. Geophys. Res.* **83**, 1740–1756 (1978).
25. G. A. Paterson, A. R. Muxworthy, Y. Yamamoto, Y. Pan, Bulk magnetic domain stability controls paleointensity fidelity. *Proc. Natl. Acad. Sci.* **114**, 13120–13125 (2017).
26. N. Suttie, J. Shaw, M. J. Hill, Direct demonstration of microwave demagnetization of a whole rock sample with minimal heating. *Earth Planet. Sci. Lett.* **292**, 357–362 (2010).
27. G. A. Paterson, L. Tauxe, A. J. Biggin, R. Shaar, L. C. Jonestrask, On improving the selection of Thellier-type paleointensity data. *Geochemistry, Geophys. Geosystems* **15**, 1180–1192 (2014).
28. R. Van der Voo, The reliability of paleomagnetic data. *Tectonophysics* **184**, 1–9 (1990).
29. G. M. Solodovnikov, Paleostrength of thegeomagnetic field in Middle-Late Carboniferous. *Izv. - Phys. Solid Earth* **28**, 327–331 (1992).
30. G. M. Solodovnikov, Geomagnetic intensity in the Middle Carboniferous of Uzbekistan. *Izv. - Russ. Acad. Sci. Phys. Solid Earth* **28**, 511–515 (1993).
31. W. E. Senanayake, M. W. McElhinny, A palaeointensity method for use with highly oxidised basalts, and application to some Permian volcanics. *J. Geophys.* **52**, 85–96 (1983).
32. A. S. Bolshakov, G. M. Solodovnikov, Y. K. Vinogradov, Paleointensity of the Geomagnetic Field in the Early Permian. *Izv. - Phys. Solid Earth*, 70–78 (1989).
33. G. M. Solodovnikov, Paleointesnity of the geomagnetic field in the Lower Permian. *Izv. - Phys. Solid Earth* **28**, 718–722 (1992).
34. J. G. Ogg, G. Ogg, F. M. Gradstein, *A concise geologic time scale 2016. [electronic book]* (2016).
35. M. Tominaga, W. W. Sager, M. A. Tivey, S.-M. Lee, Deep-tow magnetic anomaly study of the Pacific Jurassic Quiet Zone and implications for the geomagnetic polarity reversal

timescale and geomagnetic field behavior. *J. Geophys. Res. Solid Earth* **113**, B07110 (2008).
36. S. D. Burgess, S. A. Bowring, High-precision geochronology confirms voluminous magmatism before, during, and after Earth's most severe extinction. *Sci. Adv.* **1** (2015).
37. J. Hansma, *et al.*, Late Devonian carbonate magnetostratigraphy from the Oscar and Horse Spring Ranges, Lennard Shelf, Canning Basin, Western Australia. *Earth Planet. Sci. Lett.* **409**, 232–242 (2015).
38. M. W. Hounslow, Geomagnetic reversal rates following Palaeozoic superchrons have a fast restart mechanism. *Nat. Commun.* **7** (2016).
39. P. L. McFadden, M. W. McElhinny, Variations in the Geomagnetic Dipole 2: Statistical Analysis of VDMs for the Past 5 Million Years. *J. Geomagn. Geoelectr.* **34**, 163–189 (1982).
40. A. V. Smirnov, E. V. Kulakov, M. S. Foucher, K. E. Bristol, Intrinsic paleointensity bias and the long-term history of the geodynamo. *Sci. Adv.* **3** (2017).
41. R. Shaar, L. Tauxe, Instability of thermoremanence and the problem of estimating the ancient geomagnetic field strength from non-single-domain recorders. *Proc. Natl. Acad. Sci. U. S. A.* **112**, 11187–11192 (2015).
42. D. Blanco, V. A. Kravchinsky, J.-P. Valet, A. Ali, D. K. Potter, Does the Permo-Triassic geomagnetic dipole low exist? *Phys. Earth Planet. Inter.* **204**–**205**, 11–21 (2012).
43. P. Olson, H. Amit, Mantle superplumes induce geomagnetic superchrons. *Front. Earth Sci.* **3**, 1–11 (2015).
44. H. Amit, P. Olson, Lower mantle superplume growth excites geomagnetic reversals. *Earth Planet. Sci. Lett.* **414**, 68–76 (2015).
45. M. W. Hounslow, M. Domeier, A. J. Biggin, Subduction flux modulates the geomagnetic polarity reversal rate. *Tectonophysics* **742**–**743**, 34–49 (2018).

Figures and Tables

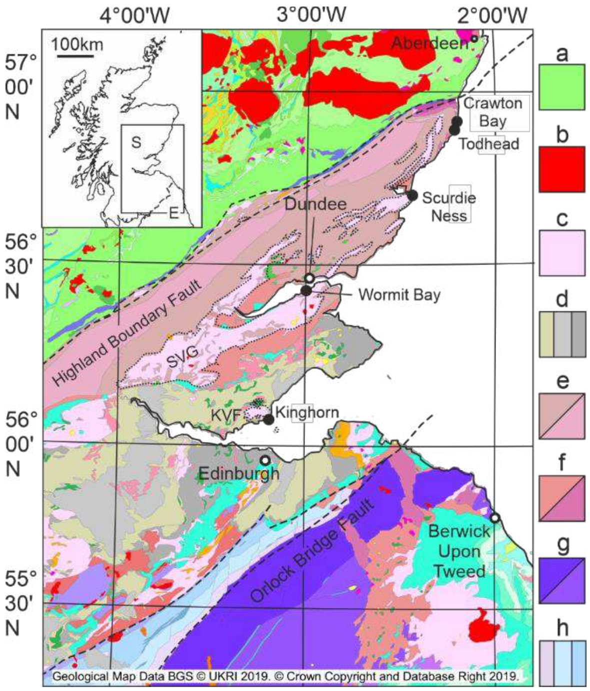

Figure 1. Geological map showing the Strathmore and Kinghorn localities used for paleodirection and paleointensity sites (site locations highlighted as black circles) in this study. The geological units come from the is the 1:50000 solid geology map from the British Geological Survey (BGS) ©UKRI 2019, accessed via Edina Digimap, and generalized descriptions are listed in the legend on the right. Key cities are highlighted as white circles and key faults as dashed lines. The Strathmore Group Volcanic (SGV) units and the Kinghorn Volcanic Formation (KVF) are highlighted with dotted outlines. The location of the geological map in outlined in the inset map in the top left corner of the Northern UK. The metamorphic and igneous geological units are a) Neoproterozoic metamorphics, b) Silurian-Early Devonian felsic intrusions, c) Silurian–Devonian mafic extrusives. The remaining units are clastic sedimentary rocks from d) Visean to Westphalian, e) Arbuthnott-Garvock/Strathmore Groups, f) other Devonian, g) Llandovery-Wenlock and h) Caradoc to Ashgill.

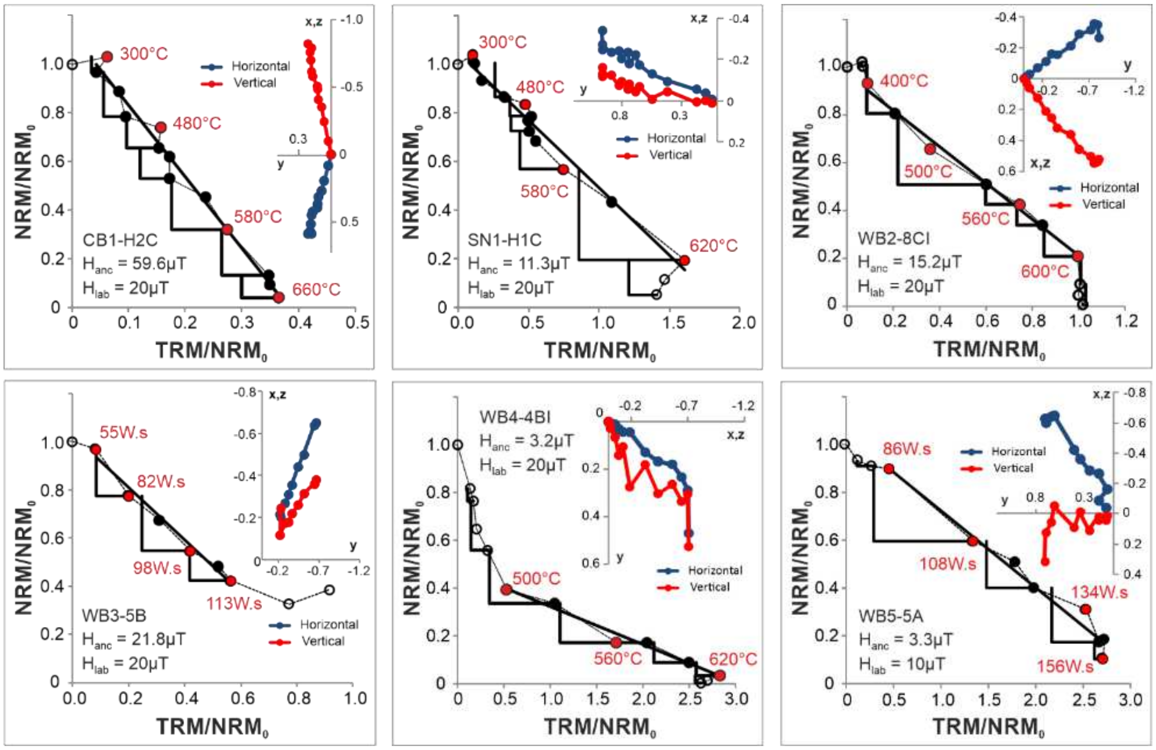

Figure 2. Representative Arai plots from the six Strathmore sites a) CB1, b) SN1, c) (WB1/)WB2, d) WB3, e) WB4 and f) WB5, illustrating the different Arai plot behaviors observed. All of the measurements were done using microwave and thermal Thellier-type experiments using the IZZI protocol, with the thermal plots showing the highlighted temperature steps (°C) and the microwave plots showing the highlighted power steps (W.s, Watts per second). The thick black lines connecting measurement steps are the pTRM checks. The corresponding orthogonal plots are inset in the top right corners of the Arai plots. Plots (a-b) are examples from the sites where there are only thermal measurements as the components come from both the magnetite and hematite temperature ranges (Fig. S2a). The remaining plots (c-f) come from the magnetite (Fig. S2b) only samples and show microwave and thermal examples from sites that have similar hysteresis properties (Fig. S2e), WB2-WB3 (c-d) and WB4-WB5 (e-f).

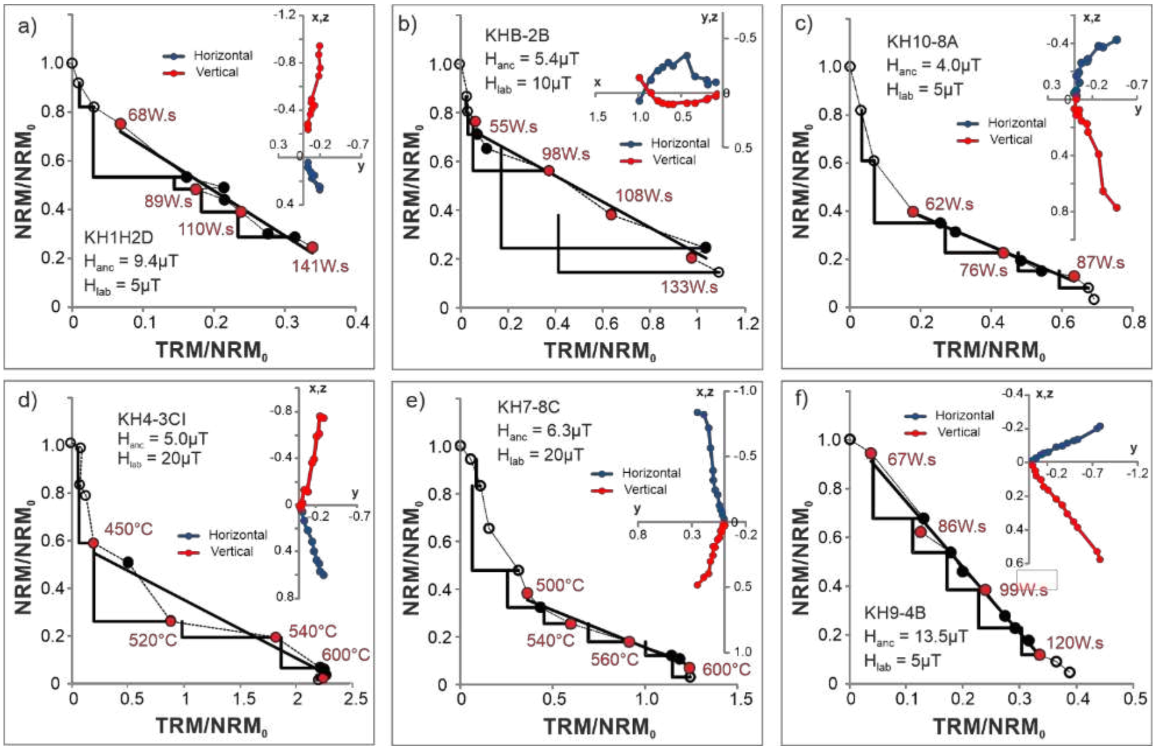

Figure 3. Representative Arai plots from six of the Kinghorn sites a) KH1, b) KHB, c) KH10, d) KH4, e) KH7 and f) KH8/9, illustrating the different Arai plot behaviors observed. All of the measurements were done using microwave and thermal Thellier-type experiments using the IZZI protocol, with the thermal plots showing the highlighted temperature steps (°C) and the microwave plots showing the highlighted power steps (W.s, Watts per second). The thick black lines connecting measurement steps are the pTRM checks. The corresponding orthogonal plots are inset in the top right corners of the Arai plots. All of the Arai plots represent (low-Ti titano-)magnetite apart from a) KH1 and b) KHB.

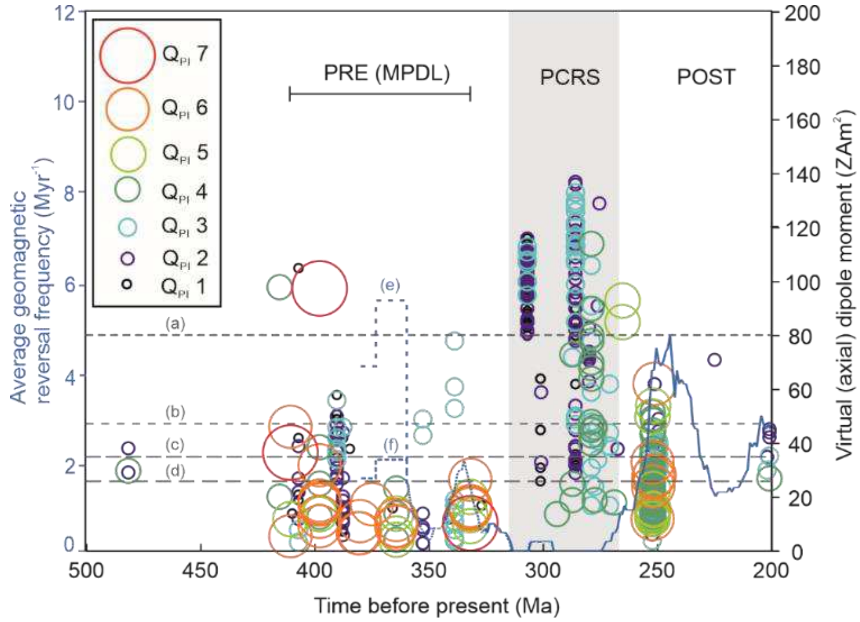

Figure 4. The age distribution of all of the V(A)DM values with Q_{PI} >0 between 200–500 Ma. A summary of the Q_{PI} scores applied to each of the studies from this period are outlined in Datasets S3 and S4. The size and the color of the circles representing the V(A)DM values corresponds to the Q_{PI} scoring as outlined in the key. The PRE-, PCRS, and POST- section refer to the same age bins used for the Kolmogorov-Smirnov tests in Figure 5 and Table S2. The dashed lines represent a) the modern field strength (39), b) CNS at Q_{PI}≥3 (11), c) JHAP Q_{PI}≥3 (11), d) JHAP Q_{PI}≥0 (11), e) the maximum possible and f) the minimum possible reversal frequency from the Canning basin magnetostratigraphy (37).

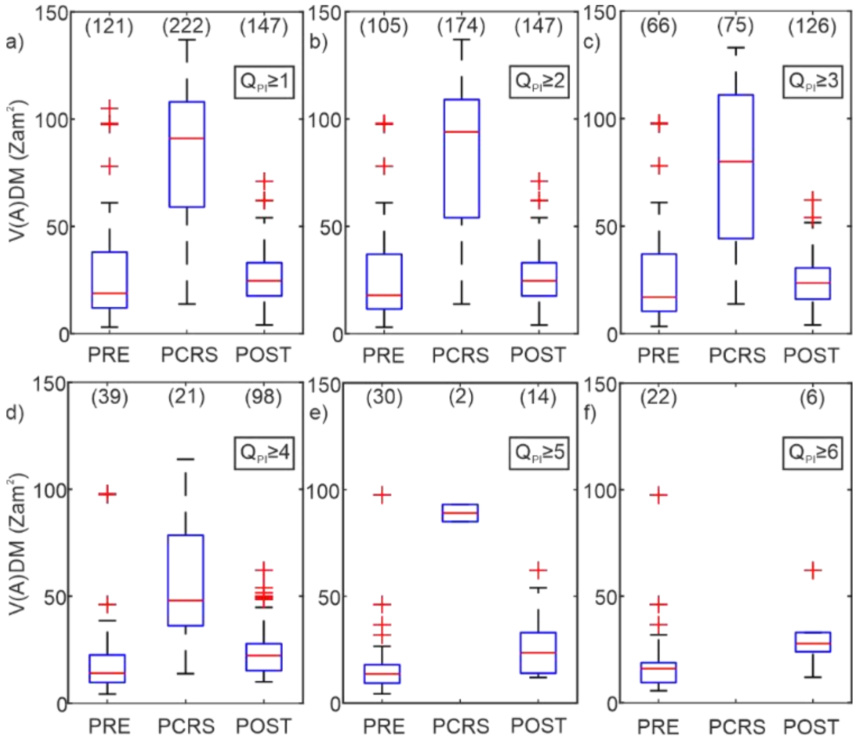

Figure 5. Boxplots showing the V(A)DM distribution of the for the different age bins used in the Kolgomorov-Smirnov tests (Table S2). The boxplots are filtered for the different Q_{PI} scores applied to the sites, between Q_{PI} ≥1 to Q_{PI} ≥6. The numbers over the boxes display the number of sites in each of the age bins. On each box, the central mark is the median, the edges of the box are the 25th and 75th percentiles, the dashed lines extend to the most extreme data points not considered outliers, and outliers are plotted individually (+).

Table 1. Summary of paleointensity results and Q_{PI} scores for all of the Strathmore and Kinghorn sites.

	Strathmore						Kinghorn							
Site	CB1	SN1	WB1/2	WB3	WB4	WB5	KH2	KH1	KHA	KHB	KH 10	KH4	KH7	KH8/9
<u>Paleointensity results:</u>														
n_{INT}	9	11	22	12	15	13	20	28	12	21	17	10	12	23
N_{INT}	5	5	11	7	5	2	6	12	3	9	4	6	4	9
N_T	5	5	8	3	2	1	1	1	-	1	-	2	1	-
N_{MW}	-	-	3	4	3	1	5	11	3	8	4	4	3	9
mean (μT)	50.9	12.6	16.8	19.7	3.1	6.3	6.6	6.1	3.7	6.7	5.2	5.3	10.9	8.6
s.d. (μT)	15.9	3.6	5.8	6.4	0.3	4.3	3.0	1.6	0.5	2.5	1.1	0.7	4.3	4.0
s.d./ mean (%)	31	29	34	32	10	68	45	26	13	38	22	13	40	47
VDM (ZAm^2)	**98.0**	**20.2**	**36.6**	**46.2**	**5.6**	**12.0**	**16.4**	**15.7**	**9.3**	**16.8**	**13.4**	**10.4**	**26.6**	**20.2**
<u>Q_{PI} scores:</u>														
AGE	1	1	1	1	1	1	1	1	1	1	1	1	1	1
STAT	0	0	0	0	1	0	0	0	0	0	0	1	0	0
TRM	0	0	1	1	1	1	1	1	1	1	1	1	1	1
ALT	1	1	1	1	1	1	1	1	1	1	1	1	1	1
MD	1	1	1	1	0	0	1	1	1	1	1	1	1	1
ACN	1	1	1	1	1	1	1	1	1	1	1	1	1	1
TECH	0	0	1	1	1	1	1	1	0	1	0	1	1	0
LITH	0	0	1	0	0	0	0	0	0	0	0	0	0	0
MAG	1	1	1	1	1	1	1	1	1	1	1	1	1	1
Q_{PI}	**5**	**5**	**8**	**7**	**7**	**6**	**7**	**7**	**6**	**7**	**6**	**8**	**7**	**6**

n_{INT}: number of samples measured; N_{INT}: number of measurements that passed selection criteria; N_T: number of accepted measurements from thermal IZZI; N_{MW}: number of measurements from microwave IZZI; s.d.: standard deviation; VDM: virtual dipole moment. The nine Q_{PI} are described in full in Biggin and Paterson (22), 1 is a pass and 0 is a fail to meet the qualitative criteria, and Q_{PI} is total score of all of these criteria. Site longitude, latitude and the corresponding site directions are available in Table S2.

Supplementary Information

Geological Background and Sampling

The older of the northern UK localities is part of the Lower "Old Red Sandstone" suite of the Strathmore region, from the northern Midland Valley in Scotland (Fig. 1). This succession is represented by interbedded fluvial conglomerates and sandstones, punctuated by calc-alkaline volcanism, and was deposited as part of three successive, graben bound sedimentary basins: the (a) Stonehaven (Stonehaven Group), (b) Crawton (Dunnotar-Crawton Group), and (c) Strathmore (Arbuthnott–Garvock and Strathmore Groups) basins (1). The magmatism originates from the subducting Laurentian plate under the Iapetus suture (2) and was greatest during the deposition of the Dunnotar-Crawton Group to the Lower Arbuthnott–Garvock Group. The sites analyzed for this study are all basaltic lava flows that come from the Crawton Volcanic Formation (Crawton Bay and Todhead) of the Dunnotar-Crawton Group and the Montrose (Scurdie Ness) and Ochil Hill (Wormit Bay) Volcanic Formations of the Arbuthnott–Garvock Group. Published Rb-Sr age dates exist from units correlated to the oldest and youngest Volcanic Formations, but there is no flow-level age data available. The Lintrathen Tuff Member of the Crawton Volcanic Formation has been correlated to the Glenbervie Porphyry member north of the highland boundary fault, which has been dated using Rb-Sr (3) and recalculated to 415.5 ± 5.8 Ma (4). For the Ochil Hills Volcanic Formation, Rb-Sr age dating was done on rhyolite from the base of the Wormit Bay section (3) and recalculated to 410.8 ± 5.6 Ma (4). This age agrees closely with misopore assemblages from the sedimentary rocks of the Wormit Bay section to the Lockhovian (419.2 ± 3.2 Ma to 410.8 ± 2.8 Ma; 5). No isotope age date exists for the Montrose Volcanic Formation, although it has been correlated with ignimbrite only 120 m stratigraphically above the top of Crawton lavas (1) and lies below the Ochil lavas.

The Kinghorn Volcanic Formation, part of the Visean volcanic sequences of Midland Valley, near Kinghorn, Scotland (Fig. 1), provided the second sample set. This formation comprises a thick sequence (~485 m) of lava flows interspersed with minor thin intercalations of sedimentary and volcanoclastic layers (6). These lava flows are predominantly olivine basalts, which approach picrite compositions in some areas (7). Thirty flows have been mapped in the region, dipping moderately (20-30 degrees) to the NE, and ranging in thickness from 2.5-12 m. Magmatism in this region is thought to be the result of lithospheric extension caused by the Variscan front to the south, which also led to rifting and the development of fault-bound basins. Stratigraphically, the age of the Kinghorn lavas are well constrained with correlations to the Sandy Craig and Pathead Formations of the Strathclyde Group, whose strata are found above and below, as well as interbedded with the Kinghorn Volcanic Formation (8). The misopore assemblages in these correlated sedimentary rocks constrain the age of the Kinghorn lavas to the Asbian-Brigantian (~337.5-326.4 Ma; 8). Isotopic age dating has been largely unsuccessful, generally underestimating ages, possibly due to Argon loss (9). The closest age date to the Asbian-Brigantian comes a K-Ar age date 338 ± 4 Ma from a sample collected between Burntisland and Kinghorn (10) but, as the paleontology appears more robust, the mean stratigraphic age is used (332.0 ± 5.6 Ma).

In this study, samples were collected from 12 visually distinct lava flows from the Strathmore locality (the Scurdie Ness lava flow boundaries were not obviously visible in the field, so sites were taken substantial distances, 100s of m, from each other) and 11 distinct lava flows from the Kinghorn locality. Sampling was done to closely mimic the sites locations used for the published paleomagnetic poles (11, 12) but could not be done precisely, as limited information on site location was included in the original publications. For the Strathmore sites, the Crawton Bay (CB) and Todhead (TH) flows are the same as those used for the published pole, the Scurdie Ness (SN) sites are from around the same location, while the Wormit Bay (WB) sites (13) are potentially new sites, being close to but not the same as the Tayside site. For the Kinghorn (KH) sites, one site was collected on Burntisland (KH2), and eleven sites were collected between Pettycur Harbour and Kinghorn Harbour (KH1, KHA-B, KH3-KH10). Note, two of the sites collected between Pettycur Harbour and Kinghorn Harbour were sampled from the same lava flow and so have been combined in analysis (KH8/9). The majority of samples were collected as oriented drill-cores, while the rest were collected as oriented hand samples that were then drilled in the laboratory. All of the samples were oriented using magnetic readings and tilt corrections were applied from bedding readings taken at locations that included sedimentary units or clear flow boundaries.

Methods

Paleodirections

All the paleodirections were obtained using stepwise thermal demagnetization. About half of these measurements (most of the samples from KH3-8, TH1-2 and WB2-5) were made using full 2.5cm cores, heated in the 24 sample Magnetic Measurements Thermal Demagnetizer (MMTD24) and measured using an Agico JR6 Spinner magnetometer. The rest came from 2.5cm cores that had been cut in half, were heated in a Super Cooled MMTD(SC) and measured on a RAPID 2G SQUID magnetometer (14). Samples were progressively heated to a maximum temperature between 580-680 °C, when the magnetic intensity of the sample had decreased to <10 % of the natural remanent magnetization (NRM). The high temperature magnetic components, interpreted as the Characteristic Remanent Magnetization (ChRM), were selected based on the orthogonal plots and calculated using principle component analysis (PCA; 14). If the mean angular dispersion (MAD°) and the angle between the anchored and unanchored directions (α°) of the individual directions were ≥ 10°, these directions were not included in the site mean analysis. Sites with dispersed, non-clustering paleodirections (k <15) were also excluded from further analysis (see Table S1). These site means are not intended to supersede previous paleomagnetic studies (as many of the site N values are fairly low) but rather to determine if the sites can reliably be used for paleointensity.

Rock magnetics

To broadly determine these sites' magnetic mineralogy, rock magnetic analysis was performed on representative specimens from each site. Hysteresis loops, isothermal remanent magnetization (IRM) and back-field curves, and thermomagnetic (Curie) curves were run in air on crushed specimens on a Magnetic Measurements Variable Field Translation Balance (MMVFTB). Scanning electron microscopy (SEM) analysis was also performed on representative sites with accepted paleointensity results using a Hitachi Table-top Microscope TM3000. Back-scattered electron (BSE) images of representative thin sections were used to confirm the presence of igneous textures, consistent with the samples carrying a primary thermoremanent magnetization (TRM). This includes looking for textures that are consistent with the rock magnetic results, such as exsolution lamellae, euhedral vs. skeletal structures, etc., and for any cracking of magnetite grains that could be consistent with a volume reduction of the grains due maghematization, which would result in a thermochemical remanent magnetization (TCRM) not suitable for paleointensity experimentation. Energy-dispersive X-ray (EDX) analysis was used, in conjunction with the BSE images, to assist in the identification of the magnetic mineralogy.

Paleointensity

Sites were deemed suitable for paleointensity analysis if they a) passed the paleodirectional selection criteria, b) had directions consistent with previous studies, and c) produced rock magnetic results that were not inconsistent with a primary TRM. Two paleointensity techniques were applied to specimens from these sites: thermal and microwave Thellier-style experiments using the "IZZI" protocol (16), starting with a zero-field (Z) step, with pTRM checks (17). Thermal experiments used oriented 2.5 cm diameter core specimens (~1 cm in height), heated in air in the super cooled MMTDSC and then measured on the RAPID 2G SQUID magnetometer. A field of 20 µT was applied along the core's Z-axis for the in-field (I) steps. An alternating field (AF) step of 5 mT was applied before measuring as an 'AF cleanse' in order to reduce any potential non-single domain (SD) effects, such as pTRM tails (18), on the paleointensity estimate (19, 20). Temperature steps were determined from the behavior of sister specimens from thermal demagnetization and the rock magnetic data. An initial temperature of 300 °C was selected to avoid low temperature overprints observed in the paleodirection data. Steps of 20–50 °C were used to a maximum of 600–660 °C, depending on the magnetic mineralogy.

Microwave experiments were performed on unoriented 5 mm diameter cores that were both (de)magnetized and measured in air using the "Tristan" 14 GHz microwave SQUID magnetometer system at the University of Liverpool (21). Each specimen is run individually, so a field of 3–20 µT, calibrated using other paleointensity estimates from each respective site, was applied, at an angle of 45–90 ° to the NRM. The selection criteria used in this study (listed in Table S2) are comparable to those used in recent studies of a similar age from Siberia (22, 23), other than the stricter FRAC cut-off used for this new study. The FRAC value (≥0.35) is still lower then recommended (24), however these suggested criteria are based on single component Arai plots. The relatively looser FRAC value used here is because, on average, the overprint on these samples represents a smaller part of the NRM then the other studies and it reduces the misfit of the site mean data, while enough estimates are accepted to still be significant.

Results

Paleodirections

Paleodirections from the Strathmore region were originally measured to determine the Devonian pole for Britain by Sallomy and Piper (25), which was then later superseded (see *Motivation* for details) by the paleomagnetic pole determined by Torsvik (12). This pole has a quality (Q) factor of seven (26), which evaluate whether seven qualitative criteria that affect the reliability of the paleomagnetic pole were addressed in the corresponding study. Rather than calculating the paleomagnetic pole by first determining the site virtual geomagnetic poles and calculating their mean, as is typical of modern studies, the Group 1 mean directions from Table III of the Torsvik study (12) were calculated with all the specimen level measurements having the same weighting. To correct for this, the mean directions from Torsvik (12) have been revised for this study by calculating the site means for from the Group 1 directions from Table II, then averaging these to get the mean directions. The revised normal, reverse and combined mean directions are included in the summary table, along with the site mean results from this study (Table S1). All but one of the site-mean directions (SN2) were reasonably well-clustered with $k > 15$ (Table S1) and agreed well with the recalculated locality means, covering both the normal and reverse field states (Fig. S1a). From the Crawton Bay flows, only CB1 has a reversed direction, which suggests that it is the same as flow 4 from the Torsvik study (12), with flows 1, 2 and 3 being CB3, CB4 and CB2 based on their relative positions. Positive conglomerate tests were obtained from the Torsvik (12) study from conglomerates underlying flow 4 (CB1) and flow 1 (CB3). Furthermore, samples taken from the conglomerate near the contact with flow 1 (within 0-0.5 m) gave similar directions to the overlying flow, suggesting it would pass a baked contact test. A conglomerate test was performed on a new site, the conglomerate overlying TH1 (site TH2), showing that directions are uniform with weak support (Fig. S1b; $P(H_A|R) = 0.71$; 27). The random nature of these directions suggests that the conglomerate has not been remagnetized but the degree of confidence is limited by the low number of samples used (n=8). A baked contact test was also performed, using a common true mean direction test between the directions from the baked sediment at Wormit Bay (WB1) and the overlying lava flow (WB2), which was positive at classification C (Angle = 7°, Critical Angle = 10°; Koymans et al., 2016; McFadden and McElhinny, 1990; Tauxe et al., 2010). The Torsvik study also reported a set of directions, which were only observed at 3 sites, including flows 1 and 2 (CB3 and CB4) and classified as Group 2 directions. Despite coming from high temperature components, the original study suggests that this near-horizontal component could be due to remagnetization (see *Results: Rock magnetics* section for discussion).

The Kinghorn paleomagnetic pole was determined by Torsvik et al. (11) and has a Q factor of 6 (31, 32). Of the nine sites sampled for directions, three failed to produce consistent directions (KH3, KH5-6), both because of individual directions failing to pass the selection criteria and the site directions not clustering. This may relate to the magnetic mineralogy of the samples (see the *Rock Magnetics* section). Unlike the Torsvik study, the majority of the lavas sampled here are normal in polarity (Fig. S1b), while the original study sampled more reversed polarity lavas to the north of the ones herein. Single oriented hand samples were collected from the remaining two sites (KHA-B) and so are not included in the directional analysis; however, the directions from oriented paleointensity measurements from these sites lie within the α_{95} circle of KH1 and have been included as part of the paleointensity analysis (Fig. S1b).

Rock magnetics

The magnetic mineralogy of the Strathmore sites can be divided into three types; two of which are potentially suitable for paleointensity analysis and one that is not. Five sites were deemed unsuitable based on the rock magnetic results (CB2-4, TH1 and SN3). These sites gave acceptable site mean paleodirections but produced rock magnetic results consistent with 'Type B' magnetic mineralogy from the Torsvik study (12). These samples gave thermomagnetic curves that are irreversible above 300 °C, with a decrease in magnetization upon alteration, and generally have a Curie temperature (T_c) of ~470–540 °C (TH1 produced a T_C of ~620–640 °C). These results are consistent with the presence of titanomaghemite, which converts into hematite when heated above 300 °C. As (titano)maghemite is only metastable (30), it is likely that some of it may have inverted into hematite at some point during the history of the sites, which may explain the high-temperature, near-horizontal directional components categorized as the Group 2 directions (12).

Both Strathmore magnetic mineralogy types deemed suitable for paleointensity analysis produced reversible thermomagnetic curves. The curves from sites CB1 and SN1 show two apparent values of T_C (Fig. S2a), the first at ~580 °C, indicative of magnetite, and second at ~680 °C, indicative of hematite. This curve is consistent with the Type C curves from Torsvik (12).

Hematite can be a primary magnetic mineral in igneous rocks but is also produced by alteration (30). However, as the paleodirections are consistent across both the magnetite and hematite temperature ranges, both are potentially primary minerals. These sites plot in the upper part of the hysteresis parameter plot in Fig. S2g, trending above and perpendicularly away from the bulk domain stability (BDS) line (33), which is consistent with the presence of hematite. The thermomagnetic curves and hysteresis properties for the baked sediment (WB1) are comparable to those from CB1 and SN1 and the hematite component likely carries a primary TRM since its direction is consistent with the overlying lava. No SEM analysis was performed on samples of this rock magnetic type.

The remaining mineralogy type deemed suitable for paleointensity analysis (sites WB2 – 5) had associated thermomagnetic curves with values of T_C from 520 to 580 °C (Fig. S2b), which correspond to the (titano-)magnetite Type A curves from Torsvik (12). SEM analysis of the samples showed grains of low- Ti (titano-)magnetite next to ilmenite, both on the order of tens of µm in length, with no finer exsolution structure apparent (Fig. S2e). All these samples plot near but just above the 'BDS' line (Fig. S2g).

The majority of the Kinghorn sites that gave acceptable paleodirections (KH2, KH4 and KH7- 9) produced reversible thermomagnetic curves with a T_C range from ~540–580 °C, indicative of low-Ti (titano-)magnetite (Fig. S2c). Sites KH1, KH10 and KHA-B, as well as all the sites that failed to give acceptable paleodirections, gave substantially lower T_C's in the range of 370–480 °C. These curves were irreversible above their respective T_C, where they increased in magnetization (Fig. S2d), which is indicative of the formation of magnetite from exsolution of the titanium-rich titano-magnetite upon heating. SEM analysis indicates the presence of very coarse exsolution structures between the titanomagnetite and ilmenite phases (Fig. S2f), with the titanomagnetite forming around the edge of large, skeletal grains of ilmenite (hundreds of µm in length). All the sites plot close to the BDS line, with moderate M_{rs}/M_s and H_{cr}/H_c values, apart from KHB, which has the lowest T_C (indicating moderate-Ti titanomagnetite), which may have affected its BDS value.

Q_{PI} Scoring

All sites pass the AGE criterion because they all have published stratigraphic and isotopic age constraints that suggest the age is reliable within reasonable errors (see *Geological Background and Sampling* for details). All but one site fail the STAT criterion, which evaluates the number of estimates (≥5) and the standard deviation of the site estimates (34). The high failure rate is likely the result of these estimates being exceptionally low. With the STAT criterion, the standard deviation is normalized using the site mean, so even small absolute differences in estimates will show up as high percent differences, when the site mean is low. In addition, most sites, from both Strathmore (CB1, SN1) and Kinghorn (KH2, KH7, and KH8/9), show a high degree of variation in the hysteresis properties (Fig S2g, h) that suggest variation of the magnetic properties of the lava flows could also be contributing to the higher standard deviation. TRM passes for all the sites, apart from the hematite bearing igneous sites (CB1, SN1), as SEM analysis is available for all of the magnetic mineralogy types apart from this one. However, the consistency between the paleodirections and paleointensity estimates from the magnetite and hematite temperature ranges support that their remanence is also likely primary. All sites passed ALT as pTRM checks were used, along with DRAT/CDRAT selection criteria, to detect alteration. As the IZZI protocol was used for all of the experiments, and any non-SD effects should present as zig-zagging in the Arai and/or accompanying orthogonal plots (16), only estimates from visually linear selected components pass MD. Sites WB4-5, however, fail MD because they exhibited zig-zagging in their orthogonal plots.

The majority of the sites passed ACN, which considers the potential effects that anisotropy of TRM, cooling rate and non-linearity of TRM have on the paleointensity estimate. All sites were considered to be unaffected by anisotropy as they had ϒ <10° (the angle between the direction of the applied field and the direction of the last pTRM acquired for the selected component), and none of the sites were considered to have been affected by cooling rate effects. The hematite bearing sites (CB1, SN1, WB1) are more likely to be affected by cooling rate because SD grains are most affected (35) and hematite tends to be SD in size (36). However, reselecting estimates, where the hematite component was included, to just below magnetite's T_C produced estimates within 15% of those selected from both components and were, in contradiction to the expected effects of cooling rate, generally higher. The rest of the sites are less likely to have been affected by cooling rate as they came from lava flows, whose hysteresis properties are consistent with non-SD grains (Fig. S2g, h). It is possible to check for this as the majority of the remaining sites included both microwave and thermal results, which have substantially different lab cooling rates (on the order of seconds for the MW and on the order of hours for thermal). All sites except WB2 and WB3 either show no systematic variation between the microwave and thermal results or the microwave estimates were lower than the thermal estimates, directly in contradiction with a cooling rate effect because they cooled quicker in the lab (37). The Kinghorn sites produced a slightly lower average paleointensity estimate for the microwave experiments (6.9 µT vs 7.7 µT). For sites, WB2 and WB3, a systematic variation was observed, with microwave results being higher than thermal results, however the cause of this variation is unclear and both sets of results suggest a relatively low field during remanence acquisition. Lastly, both the paleointensity estimates and applied field values (≤20 µT) should all be low enough that the non-linearity of TRM had no significant effect (38), so all of the sites passed ACN. Sites passed the TECH criterion where both thermal and microwave results were accepted as the two techniques use different de-/remagnetization mechanisms. The only site to pass LITH is WB1/2 as the accepted estimates come from two different lithologies with distinct magnetic mineralogy's. All the sites pass MAG as the raw data files are published alongside this study. Further details for the assigned Q_{PI} scores for these sites can be found in Dataset S4.

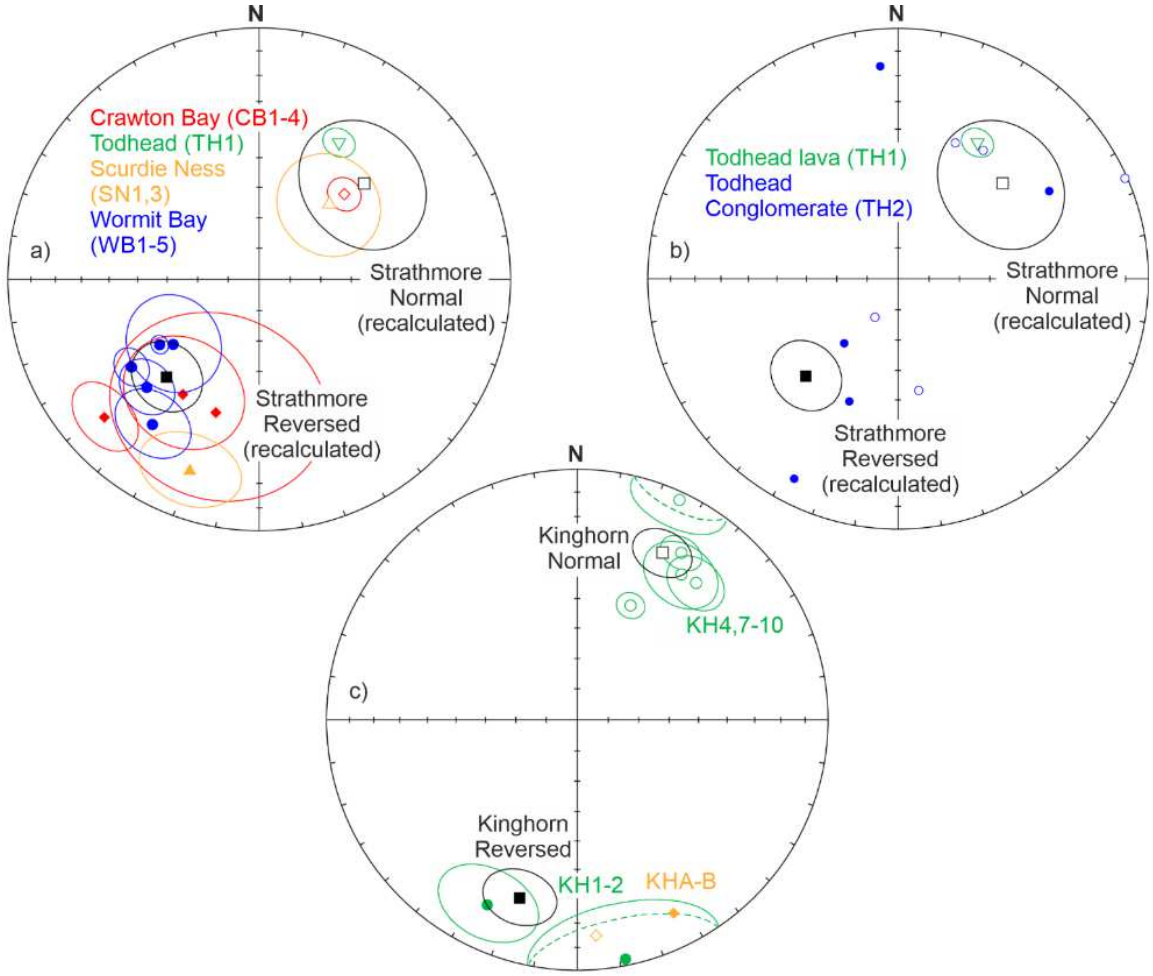

Fig. S1. Stereographic projections of (a) the accepted site mean directions from the Strathmore region, (b) the individual directions used for the conglomerate test for TH2 and (c) the accepted site mean directions from the Kinghorn lava flows. The site means are shown with their α_{95} circle. For the Strathmore site means (a), the new site directions from the different localities are represented by different colours and symbols; red diamonds (Crawton Bay), green inverted triangle (Todhead), orange triangles (Scurdie Ness) and blue circles (Wormit Bay). For the conglomerate test (b), the site mean for the TH1 lavas are as in (a) with blue circles for the individual conglomerate directions (TH2). For the Kinghorn sites (c), the new site directions are represented by green circles and the orange diamonds represent the average direction from the selected component from oriented paleointensity experiments for sites without separate paleointensity analysis. The black squares on both plots represent the locality mean directions used for the paleomagnetic poles from Torsvik (12) for Strathmore, recalculated to fit with modern paleodirectional analysis (see *Results; Paleodirections* for more details), and Torsvik et al. (11) for the Kinghorn.

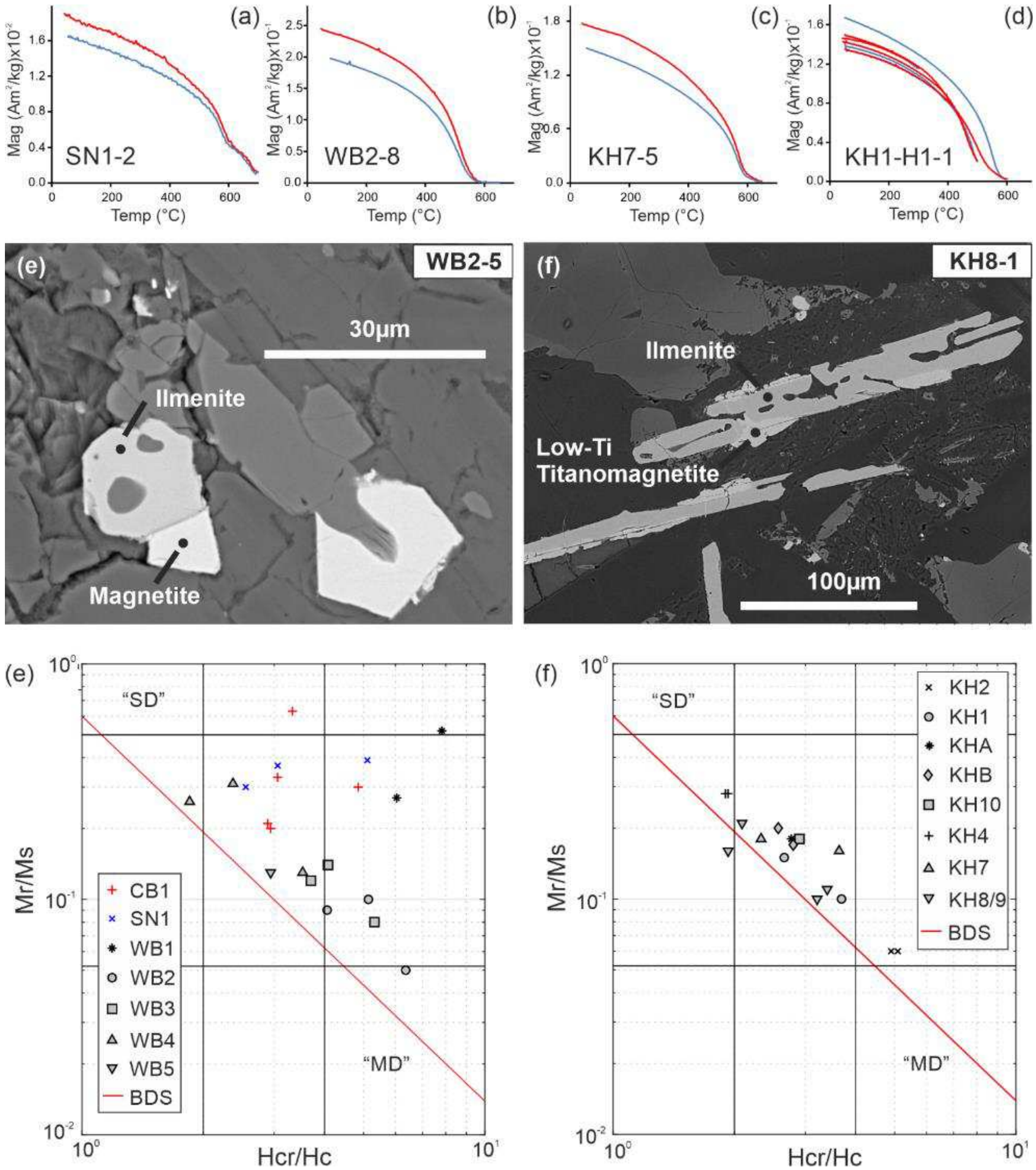

Fig. S2. Representative thermomagnetic curves (a-d), representative BSE SEM images (e-f) and (g-h) hysteresis data plotted on a H_{cr}/H_c vs. M_r/M_s or "Day" plot from the sites that provided accepted paleointensity estimates. The thermomagnetic curves show the magnetization of the sample upon heating (red curve) and cooling (blue curve). The first two thermomagnetic curves (a-b), the left SEM image (e) and the left "Day" plot (g) are representative of the Strathmore sites while the rest are representative of the Kinghorn sites. Most of the thermomagnetic curves (a-c) show a single heating or cooling curve to 600-700 °C (all of these curves are considered to be relatively reversible, while the last curve (d) in steps of 100 °C from 300 °C to show the temperature range over which the curves are (ir)reversible, indicating the presence of alteration. For the SEM images (e-f), the key magnetic minerals are labelled, having been identified from the EDX and igneous textures. The H_{cr}/H_c vs. M_r/M_s or "Day" plots (g-h) show the hysteresis data from all of the samples that provided accepted paleointensity measurements; the red bulk domain state (BDS) line comes from Paterson et al. (2017) and the black lines represent the grain size boundaries from Dunlop (2002) with the "single-domain" ("SD") and "multi-domain" ("MD") boxes highlighted.

Table S1. Summary of the accepted site and locality mean directional data from the new Strathmore and Kinghorn sites, as well as the recalculated Strathmore sites from Torsvik (12).

Site	S_{LAT} (°)	S_{LONG} (°)	N (n)	D_G (°)	I_G (°)	D_S (°)	I_S (°)	k	α_{95}	P_{LAT}
Strathmore Locality:										
Crawton Bay										
CB1	56.9080	-2.2022	11	33.5	-62.3	45.0	-50.4	71.2	5.4	-43.6
CB2	56.9077	-2.2001	7	225.6	31.1	228.3	18.4	33.7	10.5	16.8
CB3	56.9081	-2.1980	4	202.2	54.2	213.6	44.1	24.5	18.9	34.8
CB4	56.9083	-2.1992	3	184.9	50.5	198.1	43.5	15.0	33.0	31.2
Todhead										
TH1	56.8848	-2.2161	10	22.6	-51.1	30.3	-37.2	99.7	4.9	-31.8
Scurdie Ness										
SN1	56.6910	-2.4424	10	44.1	-16.0	50.6	-64.6	25.5	9.8	-8.2
SN2	56.6952	-2.4415	4	16.6	-12.9	357.6	-55.7	2.1	88.0	-6.5
SN3	56.6810	-2.4507	8	199.0	-26.7	200.0	19.8	16.7	13.9	-14.1
Wormit Bay										
WB1	56.4241	-2.9849	8	250.9	21.2	235.5	38.1	90.1	5.9	11.0
WB2	56.4244	-2.9847	8	244.8	24.8	227.1	38.3	37.1	9.2	13.0
WB3	56.4237	-2.9857	8	230.8	22.3	215.8	29.1	24.5	11.4	11.6
WB4	56.4207	-2.9911	9	261.3	36.2	234.8	55.7	18.4	12.3	20.1
WB5	56.4207	-2.9911	8	261.2	31.2	239.5	51.5	143.3	4.6	16.8
New locality means										
Normal	-	-	3	-	-	40.0	-51.1	28.5	23.5	-31.7
Reverse	-	-	9	-	-	220.5	38.5	21.4	11.4	21.7
Combined	-	-	12	-	-	220.4	41.7	22.1	9.4	24.0
Redone Torsvik locality means										
Normal	-	-	6	-	-	53.5	-45.3	13.9	24.3	-26.8
Reverse	-	-	9	-	-	223.5	45.3	11.4	21.3	26.8

Combined	-	-	15	-	-	227.5	45.4	8.1	23.0	26.9
Kinghorn locality:										
Kinghorn sites										
KH2	56.0586	-3.2233	2	209.6	5.8	205.9	18.8	318.6	14.0	2.9
KH1	56.0625	-3.1793	2	169.7	3.2	168.6	2.8	118.7	23.1	1.6
KHA*	56.0621	-3.1782	1 (4)	166.2	-3.5	166.0	4.8	7.0	37.5	2.4
KHB*	56.0622	-3.1777	1 (2)	153.6	14.9	146.5	16.3	1412.3	6.7	8.3
KH10	56.0626	-3.1749	8	24.3	8.3	24.9	-3.7	21.9	12.1	-1.8
KH3	56.0633	-3.1739	3	32.3	6.8	32.3	-7.3	2.2	121.1	3.4
KH4	56.0639	-3.1734	8	38.9	-34.1	25.0	-48.3	162.2	4.4	-18.7
KH5	56.0643	-3.1733	4	257	50.4	253.6	76.3	1.5	128.2	31.1
KH6	56.0645	-3.1730	2	39.5	43.6	48.4	28.7	5	-	25.5
KH7	56.0669	-3.1735	7	36.2	-10.0	31.9	-22.6	103.4	6.0	-5.1
KH8/9	56.0680	-3.1738	11	43.3	-14.9	38.1	-29.1	49.6	6.5	-15.5
New locality means										
Normal	-	-	4	-	-	30.1	-26.0	18.0	22.3	-13.7
Reverse	-	-	2	-	-	186.7	11.4	8.4	102.1	5.7
Combined	-	-	6	-	-	22.0	-21.6	11.9	20.2	-11.2

S_{LAT} and S_{LONG}: site longitude and latitude; N (n): Number of samples (number of specimens); D_G and I_G: (anchored) Declination and Inclination in geographic co-ordinates; D_S and I_S: (anchored) Declination and Inclination in stratigraphic co-ordinates i.e. tectonically corrected; k and α_{95}: the precision parameter and 95% confidence limit from Fisher statistics (30); P_{LAT}: Paleolatitude. The sites that have been greyed out were not included in the new locality means. For the majority of sites, this was because the site mean directions were not clustered (k <15; k values with these values are underlined, as well as high α_{95} values >45°). *These sites were not included in the locality means as the site directions came from the paleointensity measurements from a single hand sample (N=1).

Table S2. Summary of the selection criteria used for accepting paleointensity estimates.

n	FRAC	β	q	$\overrightarrow{k'}$	MAD_{ANC}	α	DRAT	CDRAT
4	≥0.35	≤0.1	≥1	<=0.48	≤15	≤15	≤15	≤15

n: number of selected measurement steps; FRAC: fraction of the NRM used for the best fit of the selected component; β: scatter around the best fit of the selected component; q: 'quality factor'; $\overrightarrow{k'}$: curvature of the selected component; MAD_{ANC}: Maximum Angular Deviation (MAD) of the (anchored) best fit direction; α: angular difference between the best-fit anchored and free-floating directions; DRAT: maximum absolute difference from a pTRM check; CDRAT: cumulative DRAT. For further details on the selection criteria, see the Standard Paleointensity Definitions (SPD; 35).

Table S3. Statistics for the PRE, PCRS and POST bins and the results of Kolmogorov-Smirnov test different levels of Q_{PI} filtering.

Statistics		Q_{PI} filter					
		Q_{PI} ≥1	**Q_{PI} ≥2**	**Q_{PI} ≥3**	**Q_{PI} ≥4**	**Q_{PI} ≥5**	**Q_{PI} ≥6**
Bin statistics:							
PRE bin statistics	***N***	121	105	66	39	30	22
	Age mean ± std.dev (skewness)	381.0 ± 29.0 (0.52)	380.1 ± 29.8 (0.69)	373.7 ± 30.4 (0.53)	380.4 ± 31.0 (0.59)	374.5 ± 27.0 (-0.18)	376.1 ± 26.4 (-0.45)
	VDM median/IQR (V%)	18.8/26.1 (139%)	17.9/25.5 (142%)	17.0/26.6 (156%)	14.1/12.8 (91%)	13.6/8.6 (63%)	16.1/9.3 (58%)
PCRS bin statistics	***N***	222	174	75	21	2	-
	Age mean ± std.dev (skewness)	290.7 ± 10.6 (-0.14)	288.7 ± 10.4 (0.12)	283.1 ± 8.4 (0.63)	279.0 ± 6.7 (-0.16)	265.4	-
	VDM median/IQR (V%)	91.0/49.0 (54%)	94.0/55.0 (59%)	80.0/66.8 (84%)	48.0/42.3 (88%)	89.0/8.0 (9%)	-
POST bin statistics	***N***	147	147	126	98	14	6
	Age mean ± std.dev (skewness)	249.2 ± 11.0 (-4.02)	249.2 ± 11.0 (-4.02)	250.6 ± 7.8 (-6.14)	251.6 ± 5.2 (-9.73)	251.9 ± 0.3 (-1.26)	251.8 ± 0.4 (-0.42)
	VDM median/IQR (V%)	24.6/15.5 (63%)	24.6/15.5 (63%)	23.6/14.5 (61%)	22.3/12.5 (56%)	23.6/19.0 (81%)	27.8/9.0 (32%)
Kolmogorov-Smirnov tests:							
p values	***PRE vs. PCRS***	2.71E-36	5.69E-30	7.94E-15	9.61E-07	2.18E-02	-
	PCRS vs. POST	4.57E-45	2.48E-40	2.21E-23	1.18E-07	1.90E-02	-
	PRE vs. POST	1.03E-03	5.46E-04	9.71E-04	4.94E-04	5.44E-02	2.27E-02
	5%	1	1	1	1	1	NaN

PRE vs. PCRS	***1%***	1	1	1	1	0	NaN
PCRS vs. POST	***5%***	1	1	1	1	1	NaN
	1%	1	1	1	1	0	NaN
PRE vs. POST	***5%***	1	1	1	1	0	1
	1%	1	1	1	1	0	0

Q_{PI}: Qualitive Paleointensity criteria defined by Biggin and Paterson (41); PRE, PCRS and POST: binned data from the updated PINT15 data (i.e. Dataset S3) from 315-416 Ma, 267-315 Ma and 200-267 Ma respectively; N: the number of site mean estimates in the bin; std. dev.: standard deviation; VDM: virtual dipole moment; IQR: interquartile range; V%: IQR/median; p: asymptotic p-values from the Kolmogorov-Smirnov (k-s) test result; 5% and 1%: the significance levels the k-s tests were performed at; 1, 0 or NaN; pass, fail or insufficient data, in one or both of the bins, for the k-s test.

Dataset S1. Summary of all the paleointensity results from the Strathmore locality. The two methods used for determining the paleointensity estimates were microwave (MW-IZZI) and thermal with an AF cleanse (TH-AF-IZZI) Thellier-type measurements using IZZI protocol with pTRM checks. The maximum and minimum steps are shown as power values listed in Watts per second (W.s) for the microwave measurements and temperature (T°C) for the thermal experiments. All of the selection criteria are described in the Standard Paleointensity Definitions (SPD) from Paterson et al. (40). Experiment results that do not pass the selection criteria are in grey and the selection criteria that failed underlined. Pi: Paleointensity estimate; H_{lab}: Applied lab field; s.d: Standard deviation.

Dataset S2. Summary of all the paleointensity results from the Kinghorn locality. The two methods used for determining the paleointensity estimates were microwave (MW-IZZI) and thermal with an AF cleanse (TH-AF-IZZI) Thellier-type measurements using IZZI protocol with pTRM checks. The maximum and minimum steps are shown as power values listed in Watts per second (W.s) for the microwave measurements and temperature (T°C) for the thermal experiments. All of the selection criteria are described in the Standard Paleointensity Definitions (SPD) from Paterson et al. (40). Experiment results that do not pass the selection criteria are in grey and the selection criteria that failed underlined. Pi: Paleointensity estimate; H_{lab}: Applied lab field; s.d: Standard deviation.

Dataset S3 (not included in this file). All of the PINT15 (42) data from between 200-500 Ma (under 'PINT data'), updated and scored for Q_{PI} ('Q_{PI} scoring'). All of the headings under 'PINT data' are consistent with the headings from the PINT15 database and explained on the 'Information' sheet (available at http://earth.liv.ac.uk/pint/). Yellow cells represent those that have been updated/added since the last upload of the PINT15 database (excel comments on the top right cell of each block describe why the changes have been made). Sites that do not have a 'Data' number have either superseded previous sites (sites that have been superseded since the last PINT update are included at the bottom of the sheet in red) or have been added from studies published since the last update. The description for Dataset S4 gives the full refence for sites with a letter ref (a-e). The 'Q_{PI} scoring' headings are consistent with names of the nine different criteria, which are explained in detail in Biggin and Paterson (41), and the final Q_{PI} score ('Q_{PI}') is the sum of all of the criteria (these are scored a 1 is they pass the criteria and 0 if they do not). The explanation for each of the site scores is given under the corresponding headings in Dataset S4.

Dataset S4 (not included in this file). Summary of the Q_{PI} scoring of all of the sites from the updated PINT15 database (42) from between 200-500 Ma (i.e. Dataset S3). The 'Study' is given in the format of first author_publication year. The 'PINTref' number corresponds to the 'REF' in PINT15 (letters are for studies added in the Dataset S3 update) and 'N' is the number of sites included in the study. The abbreviations used in 'Method' are consistent with those on the 'PI Methods' sheet of the PINT15 database. The headings under 'Q_{PI} Values' are consistent with the nine Q_{PI} criteria which are explained in detail in Biggin and Paterson (41), and the final Q_{PI} score ('Q_{PI}') is the sum of all of the criteria (these are scored a 1 is they pass the criteria and 0 if they do not). Cells with the same headings under 'Notes' provide explanations for the site scorings for the first eight criteria (MAG only passes only when the raw data is published e.g. in the studies supplementary information, on the MAGIC database, etc.). 'Other Notes' provides other information such as the revision of age dates based on newly published ages, how sites have been recalculated, why certain QPI criteria have been rescored since previously being published, etc.

*a) Shcherbakova et al, 2015 (43), b) Anwar et al, 2016 (44), c) Shcherbakova et al, 2017 (23), d) Usui and Tian, 2017 (45) and e) Hawkins et al., 2019 (22).

Supplementary References

1. M. Browne, R. Smith, A. M. Aitken, "Stratigraphical framework for the Devonian (Old Red Sandstone) rocks of Scotland south of a line from Fort William to Aberdeen" (2002).
2. N. H. Woodcock, "Early Devonian Sedimentary and Magmatic Interlude after Iapetus Closure" in *Geological History of Britain and Ireland*, Wiley Online Books., (2012), pp. 193–209.
3. M. F. Thirlwall, Isotope geochemistry and origin of calc-alkaline lavas from a caledonian continental margin volcanic arc. *J. Volcanol. Geotherm. Res.* **18**, 589–631 (1983).
4. M. F. Thirlwall, Geochronology of Late Caledonian magmatism in northern Britain. *J. Geol. Soc. London.* **145**, 951–967 (1988).
5. J. B. Richardson, J. H. Ford, F. Parker, Miospores, correlation and age of some Scottish Lower Old Red Sandstone sediments from the Strathmore region (Fife and Angus). *J. Micropalaeontology* **3**, 109–124 (1984).
6. D. Stephenson, S. C. Loughlin, D. Millward, C. N. Waters, I. T. Williamson, *Carboniferous and Permian Igneous Rocks of Great Britain North of the Variscan Front* (Joint Nature Conservation Commitee, 2003).
7. A. Geikie, *The geology of central and western Fife and Kinross* (Mem. Geol. Surv. Scotland, 1900).
8. S. Brindley, E. Spinner, Palynological assemblages from Lower Carboniferous deposits, Burntisland district, Fife, Scotland. *Proc. Yorksh. Geol. Soc.* **47**, 215–231 (1989).
9. A. A. Monaghan, M. A. E. Browne, "Nine 40Ar/39Ar dates from Carboniferous igneous rocks of the Midland Valley of Scotland" (2010).
10. F. J. Fitch, J. A. Miller, S. C. Williams, Isotopic ages of British Carboniferous rocks. *C.r. 6th Int. Congr. Carb. Strat. Geol. (Sheffield, 1967)* **2**, 771–789 (1970).
11. T. H. Torsvik, O. Lyse, G. Atterás, B. J. Bluck, Palaeozoic palaeomagnetic results from Scotland and their bearing on the British apparent polar wander path. *Phys. Earth Planet. Inter.* **55**, 93–105 (1989).
12. T. H. Torsvik, Magnetic properties of the Lower Old Red Sandstone lavas in the Midland Valley, Scotland; palaeomagnetic and tectonic considerations. *Phys. Earth Planet. Inter.* **39**, 194–207 (1985).
13. D. Stephenson, *et al.*, *Caledonian Igneous Rocks of Great Britain* (Joint Nature Conservation Commitee, 1999).
14. J. L. Kirschvink, R. E. Kopp, T. D. Raub, C. T. Baumgartner, J. W. Holt, Rapid, precise, and high-sensitivity acquisition of paleomagnetic and rock-magnetic data: Development of a low-noise automatic sample changing system for superconducting rock magnetometers. *Geochemistry, Geophys. Geosystems* **9** (2008).
15. J. L. Kirschvink, The least-squares line and plane and the analysis of palaeomagnetic data. *Geophys. Journal, R. Astron. Soc.* **62**, 699–718 (1980).
16. Y. Yu, L. Tauxe, Testing the IZZI protocol of geomagnetic field intensity determination. *Geochemistry, Geophys. Geosystems* **6** (2005).
17. R. S. Coe, S. Grommé, E. A. Mankinen, Geomagnetic paleointensities from radiocarbon-dated lava flows on Hawaii and the question of the Pacific nondipole low. *J. Geophys. Res.* **83**, 1740–1756 (1978).
18. S. Levi, The effect of magnetite particle size on paleointensity determinations of the geomagnetic field. *Phys. Earth Planet. Inter.* **13**, 245–259 (1977).
19. D. J. Dunlop, Ö. Özdemir, Beyond Néel's theories: Thermal demagnetization of narrow-

band partial thermoremanent magnetizations. *Phys. Earth Planet. Inter.* **126**, 43–57 (2001).
20. A. Biggin, M. Perrin, J. Shaw, A comparison of a quasi-perpendicular method of absolute palaeointensity determination with other thermal and microwave techniques. *Earth Planet. Sci. Lett.* **257**, 564–581 (2007).
21. M. J. Hill, Y. Pan, C. J. Davies, An assessment of the reliability of palaeointensity results obtained from the Cretaceous aged Suhongtu section, Inner Mongolia, China. *Phys. Earth Planet. Inter.* **169**, 76–88 (2008).
22. L. M. A. Hawkins, *et al.*, An exceptionally weak Devonian geomagnetic field recorded by the Viluy Traps, Siberia. *Earth Planet. Sci. Lett.* **506**, 134–145 (2019).
23. V. V. Shcherbakova, *et al.*, Was the Devonian geomagnetic field dipolar or multipolar? Palaeointensity studies of Devonian igneous rocks from the Minusa Basin (Siberia) and the Kola Peninsula dykes, Russia. *Geophys. J. Int.* **209**, 1265–1286 (2017).
24. G. A. Paterson, A. J. Biggin, E. Hodgson, M. J. Hill, Thellier-type paleointensity data from multidomain specimens. *Phys. Earth Planet. Inter.* **245**, 117–133 (2015).
25. J. T. Sallomy, J. D. A. Piper, Palaeomagnetic Studies in the British Caledonides - IV Lower Devonian Lavas of the Strathmore Region. *Geophys. Journal, R. Astron. Soc.* **34**, 47–68 (1973).
26. B. Steinberger, T. H. Torsvik, A geodynamic model of plumes from the margins of Large Low Shear Velocity Provinces. *Geochemistry, Geophys. Geosystems* **13** (2012).
27. D. Heslop, A. P. Roberts, A Bayesian Approach to the Paleomagnetic Conglomerate Test. *J. Geophys. Res. Solid Earth* **123**, 1132–1142 (2018).
28. M. R. Koymans, C. G. Langereis, D. Pastor-Galán, D. J. J. van Hinsbergen, Paleomagnetism.org: An online multi-platform open source environment for paleomagnetic data analysis. *Comput. Geosci.* **93**, 127–137 (2016).
29. P. L. McFadden, M. W. McElhinny, Classification of the reversal test in palaeomagnetism. *Geophys. J. Int.* **103**, 725–796 (1990).
30. L. Tauxe, R. F. Butler, R. Van der Voo, S. K. Banerjee, *Essentials of paleomagnetism.* (University of California Press, 2010).
31. R. Van der Voo, The reliability of paleomagnetic data. *Tectonophysics* **184**, 1–9 (1990).
32. T. H. Torsvik, *et al.*, Phanerozoic polar wander, palaeogeography and dynamics. *Earth-Science Rev.* **114**, 325–368 (2012).
33. G. A. Paterson, A. R. Muxworthy, Y. Yamamoto, Y. Pan, Bulk magnetic domain stability controls paleointensity fidelity. *Proc. Natl. Acad. Sci.* **114**, 13120–13125 (2017).
34. G. A. Paterson, D. Heslop, A. R. Muxworthy, Deriving confidence in paleointensity estimates. *Geochemistry, Geophys. Geosystems* **11** (2010).
35. A. J. Biggin, S. Badejo, A. R. Muxworthy, M. J. Dekkers, The effect of cooling rate on the intensity of thermoremanent magnetization (TRM) acquired by assemblages of pseudo-single domain, multidomain and interacting single-domain grains. *Geophys. J. Int.* **193**, 1239–1249 (2013).
36. G. Kletetschka, P. J. Wasilewski, Grain size limit for SD hematite. *Phys. Earth Planet. Inter.* **129**, 173–179 (2002).
37. S. L. Halgedahl, R. Day, M. Fuller, The effect of cooling rate on the intensity of weak-field TRM in single- domain magnetite. *J. Geophys. Res.* **85**, 3690–3698 (1980).
38. P. A. Selkin, J. S. Gee, L. Tauxe, Nonlinear thermoremanence acquisition and implications for paleointensity data. *Earth Planet. Sci. Lett.* **256**, 81–89 (2007).

39. D. J. Dunlop, Theory and application of the Day plot (Mrs/Ms versus Hcr/Hc) 1. Theoretical curves and tests using titanomagnetite data. *J. Geophys. Res. Solid Earth* **107** (2002).
40. G. A. Paterson, L. Tauxe, A. J. Biggin, R. Shaar, L. C. Jonestrask, On improving the selection of Thellier-type paleointensity data. *Geochemistry, Geophys. Geosystems* **15**, 1180–1192 (2014).
41. A. J. Biggin, G. A. Paterson, A new set of qualitative reliability criteria to aid inferences on palaeomagnetic dipole moment variations through geological time. *Front. Earth Sci.* **2**, 1–9 (2014).
42. A. J. Biggin, G. H. M. A. Strik, C. G. Langereis, The intensity of the geomagnetic field in the late-Archaean: New measurements and an analysis of the updated IAGA palaeointensity database. *Earth, Planets Sp.* **61**, 9–22 (2009).
43. V. V. Shcherbakova, G. V. Zhidkov, V. P. Shcherbakov, A. V. Latyshev, A. M. Fetisova, Verifying the mesozoic dipole low hypothesis by the Siberian trap data. *Izv. Phys. Solid Earth* **51**, 47–67 (2015).
44. T. Anwar, L. Hawkins, V. A. Kravchinsky, A. J. Biggin, V. E. Pavlov, Microwave paleointensities indicate a low paleomagnetic dipole moment at the Permo-Triassic boundary. *Phys. Earth Planet. Inter.* **260**, 62–73 (2016).
45. Y. Usui, W. Tian, Paleomagnetic directional groups and paleointensity from the flood basalt in the Tarim large igneous province: Implications for eruption frequency. *Earth, Planets Sp.* **69** (2017).

Dataset S1:

Sample details				Paleointensity component				Selection criteria													Site mean results			
Location	Site	Sample	Method	Low T (°C)/W.s	High T (°C)/W.s	Pi (μT)	H_{lab} (μT)	n	β	FRAC	g	q	δCK	DRAT	CDRAT	α	MAD_{ANC}	Υ	$\vec{k'}$	npTRM	N	Mean Pi (μT)	s.d. (μT)	s.d./ Mean Pi
Crawton Bay	CB1	CB1-1CII	TH-AF-IZZI	300	540	52.3	20	8	0.128	0.678	0.838	3.6	8.6%	5.6%	-7.2%	10.6	4.5	2.5	0.26	4				
Crawton Bay	CB1	CB1-2CII	TH-AF-IZZI	300	520	45.5	20	7	0.142	0.584	0.801	3.1	6.2%	4.5%	5.5%	8.7	3.4	4	0.60	3				
Crawton Bay	CB1	CB1-3BII	TH-AF-IZZI	300	540	64.7	20	8	0.082	0.688	0.816	5.0	13.3%	7.8%	-12.6%	12.2	5.8	2.4	0.13	4				
Crawton Bay	CB1	CB1-4BII	TH-AF-IZZI	450	620	15.7	20	8	0.153	0.436	0.794	4.1	5.6%	5.6%	5.6%	4.6	2.8	3.4	0.84	6				
Crawton Bay	CB1	CB1-5CII	TH-AF-IZZI	500	620	18.8	20	6	0.201	0.310	0.683	2.2	6.1%	6.7%	7.0%	3.1	2.1	1.4	0.89	6	5	50.9	15.9	31%
Crawton Bay	CB1	CB1-6CII	TH-AF-IZZI	300	640	27.9	20	12	0.059	0.889	0.866	11.3	6.7%	5.1%	-8.7%	2.5	2.6	3.9	0.35	6				
Crawton Bay	CB1	CB1-H1B	TH-AF-IZZI	300	640	61.5	20	12	0.079	0.825	0.880	7.8	16.4%	7.2%	-4.5%	1.1	1.3	2	-0.35	6				
Crawton Bay	CB1	CB1-H2C	TH-AF-IZZI	300	660	59.6	20	13	0.045	0.924	0.876	16.4	12.7%	4.8%	-9.8%	0.7	1.1	2.6	0.09	7				
Crawton Bay	CB1	CB1-H4AI	TH-AF-IZZI	300	560	40.8	20	9	0.072	0.783	0.862	8.5	12.5%	7.8%	-8.7%	6.1	3.3	1.3	0.16	4				
Scurdie Ness	SN1	SN1-1BII	TH-AF-IZZI	500	620	11.9	20	7	0.044	0.569	0.696	11.8	5.9%	6.9%	6.4%	4.0	2.2	4.2	0.33	6				
Scurdie Ness	SN1	SN1-1A	MW-IZZI								Sample broke early in the experiment													
Scurdie Ness	SN1	SN1-2BII	TH-AF-IZZI	540	640	12.5	20	6	0.058	0.384	0.673	5.6	3.0%	5.3%	2.9%	5.7	2.3	1.1	-0.08	6				
Scurdie Ness	SN1	SN1-3BII	TH-AF-IZZI	300	580	18.5	20	10	0.090	0.332	0.841	2.9	1.8%	4.4%	-4.7%	14.4	2.1	2.6	0.46	5				
Scurdie Ness	SN1	SN1-4CI	TH-AF-IZZI	350	580	8.9	20	9	0.071	0.544	0.631	4.9	10.4%	17.4%	22.1%	8.1	2.5	3.0	0.33	5				
Scurdie Ness	SN1	SN1-5BII	TH-AF-IZZI	300	480	9.2	20	5	0.139	0.469	0.581	1.8	3.2%	6.8%	6.0%	3.7	2.9	4.1	-0.24	2	5	12.6	3.6	29%
Scurdie Ness	SN1	SN1-H1C	TH-AF-IZZI	300	620	11.4	20	12	0.053	0.784	0.825	12.7	7.9%	8.5%	3.0%	4.3	2.8	0.3	0.24	6				
Scurdie Ness	SN1	SN1-H2AI	TH-AF-IZZI	300	450	18.5	20	4	0.040	0.383	0.526	9.1	10.3%	11.0%	4.6%	6.0	5.2	3.7	0.07	2				
Scurdie Ness	SN1	SN1-H3CI	TH-AF-IZZI	300	450	12.5	20	4	0.167	0.274	0.531	1.6	10.0%	16.9%	-12.7%	19.8	10.3	3.3	1.01	2				
Scurdie Ness	SN1	SN1-H4BI	TH-AF-IZZI	350	620	8.6	20	11	0.058	0.772	0.859	11.9	11.3%	12.9%	10.3%	3.9	3.4	6.7	0.13	6				
Scurdie Ness	SN1	SN1-H5AI	TH-AF-IZZI	300	450	13.1	20	4	0.184	0.566	0.511	1.9	16.0%	19.4%	13.6%	8.8	4.5	3.9	0.89	2				
Wormit Bay	WB1	WB1-H1-1	TH-AF-IZZI	350	640	19.9	20	11	0.036	0.298	0.852	11.1	8.2%	12.4%	0.7%	2.3	2.3	2.3	0.24	6				
Wormit Bay	WB1	WB1-H3-1	TH-AF-IZZI	300	640	20.4	20	12	0.028	0.427	0.875	16.6	8.0%	10.7%	-3.9%	3.1	2.3	3.5	0.04	6				
Wormit Bay	WB1	WB1-H5-1	TH-AF-IZZI	300	660	26.8	20	13	0.022	0.705	0.880	22.1	4.1%	4.4%	0.9%	5.6	2.8	5.4	0.18	7				
Wormit Bay	WB1	WB1-H6-1	TH-AF-IZZI	400	640	17.7	20	10	0.046	0.350	0.809	7.5	11.0%	19.5%	-32.2%	2.9	2.0	2.9	-0.06	6				
Wormit Bay	WB1	WB1-H7-1	TH-AF-IZZI	300	660	16.2	20	13	0.086	0.408	0.880	3.8	7.3%	15.4%	-20.1%	5.2	6.5	1.1	-0.51	7				
Wormit Bay	WB1	WB1-H8-1	TH-AF-IZZI	400	640	21.5	20	10	0.081	0.300	0.839	2.4	7.4%	21.4%	-32.5%	3.5	3.6	2.6	0.20	6				
Wormit Bay	WB2	WB2-1CI	TH-AF-IZZI	300	450	17.4	20	4	0.008	0.596	0.293	21.6	3.9%	4.7%	8.2%	6.8	3.0	1.5	0.06	2				
Wormit Bay	WB2	WB2-3CII	TH-AF-IZZI	300	470	21.0	20	5	0.046	0.666	0.605	8.8	2.8%	2.9%	1.9%	3.6	2.6	2.7	0.22	2				
Wormit Bay	WB2	WB2-4CI	TH-AF-IZZI	300	450	20.3	20	4	0.032	0.602	0.197	3.8	0.8%	1.0%	-0.7%	5.8	2.5	1.5	0.46	2				
Wormit Bay	WB2	WB2-5AI	TH-AF-IZZI	300	540	19.8	20	6	0.031	0.792	0.650	14.3	4.7%	4.9%	-5.7%	6.5	4.3	2.6	-0.11	3				
Wormit Bay	WB2	WB2-5B	MW-IZZI	0	41	4.2	20	3	0.168	0.093	0.476	0.1	0.4%	9.1%	-9.1%	71.1	3.3	8.6	-0.08	1				
Wormit Bay	WB2	WB2-5C	MW-IZZI	41	105	15.6	20	6	0.126	0.551	0.729	2.8	6.2%	9.9%	-10.7%	3.2	6.9	3	0.25	3	11	16.8	5.8	34%
Wormit Bay	WB2	WB2-5D	MW-IZZI	46	114	10.5	15	7	0.093	0.639	0.761	5.2	2.2%	2.9%	-4.5%	10.3	4.8	2.3	0.25	3				
Wormit Bay	WB2	WB2-5E	MW-IZZI	39	96	14.8	10	5	0.097	0.393	0.651	2.8	2.7%	3.7%	1.9%	8.8	2.9	5.2	0.67	3				
Wormit Bay	WB2	WB2-5F	MW-IZZI	82	112	6.4	20	6	0.048	0.481	0.656	5.9	4.4%	9.7%	-2.7%	7.7	6.8	2.8	0.28	4				
Wormit Bay	WB2	WB2-6CII	TH-AF-IZZI	300	470	14.3	20	5	0.097	0.592	0.704	4.2	3.7%	5.2%	5.1%	4.5	2.7	0.8	0.48	2				
Wormit Bay	WB2	WB2-7BII	TH-AF-IZZI	300	540	15.7	20	8	0.022	0.803	0.787	25.3	8.9%	9.7%	11.3%	4.1	3.6	1.9	-0.12	4				
Wormit Bay	WB2	WB2-8CI	TH-AF-IZZI	400	600	15.2	20	7	0.039	0.649	0.824	15.2	1.5%	1.6%	1.8%	3.7	2.5	3.8	0.11	6				
Wormit Bay	WB2	WB2-8B	MW-IZZI	20	135	15.1	15	8	0.089	0.624	0.804	5.2	9.7%	11.9%	-19.4%	15.3	5.8	5.5	0.47	4				
Wormit Bay	WB2	WB28CB	MW-IZZI	63	146	11.2	15	9	0.038	0.572	0.833	15.0	9.5%	11.3%	-6.6%	11.3	6.2	1.3	-0.20	5				
Wormit Bay	WB2	WB28CC	MW-IZZI	63	111	7.0	15	6	0.051	0.610	0.759	9.5	15.3%	21.7%	38.0%	11.8	9.1	7.4	-0.15	3				
Wormit Bay	WB2	WB28CD	MW-IZZI	42	119	12.3	20	8	0.062	0.587	0.835	7.6	9.7%	14.7%	25.3%	3.7	3.2	6.1	0.02	4				
Wormit Bay	WB3	WB3-1BI	TH-AF-IZZI	540	620	10.0	20	4	0.048	0.328	0.578	10.9	17.3%	16.9%	-3.3%	0.4	0.9	2.5	0.08	7				
Wormit Bay	WB3	WB3-2BI	TH-AF-IZZI	300	540	18.2	20	6	0.101	0.624	0.713	4.7	8.1%	9.0%	11.6%	9.3	4.0	2.9	0.59	3				
Wormit Bay	WB3	WB3-4CI	TH-AF-IZZI	540	620	10.6	20	5	0.039	0.429	0.538	12.2	17.9%	17.7%	9.2%	0.4	2.0	2.0	-0.07	7				
Wormit Bay	WB3	WB3-5BI	TH-AF-IZZI	350	540	28.1	20	5	0.051	0.652	0.685	8.6	2.0%	1.8%	-1.2%	4.8	2.5	3.6	-0.10	3				
Wormit Bay	WB3	WB3-5A	MW-IZZI	67	117	19.1	15	5	0.045	0.542	0.732	8.7	2.0%	2.3%	-2.1%	0.2	0.7	1.0	0.07	2				
Wormit Bay	WB3	WB3-5B	MW-IZZI	56	99	21.9	20	6	0.067	0.464	0.778	6.0	5.2%	6.7%	6.5%	1.9	1.0	2.3	0.36	3				
Wormit Bay	WB3	WB3-6BI	TH-AF-IZZI	300	540	22.8	20	6	0.067	0.730	0.671	7.5	2.4%	2.1%	2.2%	5.2	3.3	4.7	0.44	3	7	19.7	6.4	32%
Wormit Bay	WB3	WB3-6A	MW-IZZI	2	7	12.4	20	6	0.088	0.489	0.797	5.7	4.2%	5.8%	-8.1%	3.7	3.7	1.0	0.16	3				
Wormit Bay	WB3	WB3-6B	MW-IZZI	4	11	10.1	20	8	0.065	0.532	0.809	7.9	6.4%	9.1%	-7.3%	3.0	4.6	1.1	0.28	5				
Wormit Bay	WB3	WB3-7BII	TH-AF-IZZI	300	500	23.5	20	6	0.032	0.760	0.657	15.5	8.3%	7.2%	11.5%	3.6	3.0	4.0	0.16	3				
Wormit Bay	WB3	WB3-8CI	TH-AF-IZZI	300	500	7.9	20	5	0.204	0.387	0.727	2.1	10.6%	16.4%	15.3%	6.6	5.1	2.3	1.02	2				
Wormit Bay	WB3	WB3-9BI	TH-AF-IZZI	300	500	6.3	20	5	0.236	0.397	0.724	1.9	10.2%	15.4%	15.0%	11.2	6.0	0.8	1.14	2				
Wormit Bay	WB4	WB4-1BI	TH-AF-IZZI	350	620	1.5	20	9	0.168	0.791	0.663	3.2	3.0%	3.7%	-0.2%	31.4	19.6	1.2	-0.05	7				
Wormit Bay	WB4	WB4-2BI	TH-AF-IZZI	450	620	2.1	20	7	0.130	0.585	0.760	4.6	3.3%	4.1%	3.1%	13.2	14.7	0.8	0.01	7				
Wormit Bay	WB4	WB4-2B	MW-IZZI	43	119	6.3	2	7	0.132	0.437	0.601	2.3	5.3%	3.1%	-4.7%	7.9	4.7	10.8	0.63	3				
Wormit Bay	WB4	WB4-2C	MW-IZZI								Altered early, no selectable component													
Wormit Bay	WB4	WB4-3A	MW-IZZI	66	127	3.0	5	6	0.059	0.500	0.722	8.1	4.6%	6.0%	6.0%	1.7	2.2	3.2	0.29	4				
Wormit Bay	WB4	WB4-3B	MW-IZZI	70	127	2.6	5	6	0.021	0.513	0.711	19.2	4.1%	6.2%	-6.6%	7.9	4.9	4.0	0.03	4				
Wormit Bay	WB4	WB4-3DI	TH-AF-IZZI	470	600	2.1	20	7	0.102	0.526	0.765	5.5	6.8%	9.2%	11.6%	12.9	13.3	5.8	0.19	5				
Wormit Bay	WB4	WB4-4BI	TH-AF-IZZI	500	620	3.2	20	6	0.072	0.405	0.750	7.8	2.6%	3.5%	8.3%	8.2	13.5	1.6	0.09	7	5	3.1	0.3	10%
Wormit Bay	WB4	WB4-4A	MW-IZZI	75	124	3.3	3	5	0.085	0.498	0.737	4.8	3.9%	4.7%	-5.9%	10.3	4.4	3.1	-0.31	3				
Wormit Bay	WB4	WB4-5BI	TH-AF-IZZI	450	640	2.4	20	8	0.098	0.554	0.789	7.2	5.4%	6.0%	8.8%	12.6	18.0	1.9	0.37	7				
Wormit Bay	WB4	WB4-5A	MW-IZZI	66	93	6.2	3	3	0.008	0.327	0.499	23.5	0.4%	0.4%	0.4%	15.7	5.6	1.0	-0.03	1				
Wormit Bay	WB4	WB4-6AI	TH-AF-IZZI	450	640	2.6	20	8	0.097	0.420	0.790	7.4	8.8%	9.6%	16.3%	11.3	16.2	1.6	0.30	7				
Wormit Bay	WB4	WB4-7BI	TH-AF-IZZI	450	640	2.2	20	8	0.086	0.530	0.811	8.2	7.8%	8.9%	15.3%	13.7	16.4	3.1	0.27	7				
Wormit Bay	WB4	WB4-H2AI	TH-AF-IZZI	470	600	3.4	20	7	0.097	0.378	0.752	5.9	2.3%	3.0%	-5.7%	8.4	7.4	2.8	-0.05	5				
Wormit Bay	WB4	WB4-H3BI	TH-AF-IZZI	520	600	4.9	20	5	0.110	0.261	0.602	3.3	2.4%	4.0%	-6.5%	1.8	2.7	3.2	0.58	5				
Wormit Bay	WB5	WB5-1BII	TH-AF-IZZI	300	470	23.1	20	5	0.109	0.238	0.691	2.5	6.4%	10.6%	-12.4%	21.4	6.8	1.7	0.73	2				
Wormit Bay	WB5	WB5-2CII	TH-AF-IZZI	350	470	6.3	20	4	0.173	0.134	0.573	0.7	4.2%	18.4%	-17.1%	54.7	6.8	2.4	-0.10	2				
Wormit Bay	WB5	WB5-3BII	TH-AF-IZZI	350	470	7.8	20	4	0.118	0.183	0.548	1.4	3.6%	11.4%	-3.7%	39.5	8.3	1.4	-0.14	2				
Wormit Bay	WB5	WB5-4CII	TH-AF-IZZI	470	580	2.4	20	6	0.157	0.482	0.647	2.5	10.5%	16.9%	15.7%	29.7	13.9	1.4	0.99	5				
Wormit Bay	WB5	WB5-5CII	TH-AF-IZZI	440	620	2.4	20	9	0.050	0.675	0.743	12.9	16.3%	18.5%	17.2%	10.9	16.3	1.9	0.30	6				
Wormit Bay	WB5	WB5-5A	MW-IZZI	86	156	3.3	10	8	0.066	0.685	0.768	8.3	5.8%	7.7%	11.5%	6.3	8.3	4.7	-0.15	5				
Wormit Bay	WB5	WB5-5B	MW-IZZI								Experiment failed										2	6.3	4.3	68%
Wormit Bay	WB5	WB5-6BII	TH-AF-IZZI	500	620	3.9	20	7	0.032	0.533	0.717	16.7	17.4%	22.6%	22.9%	3.0	8.7	2.5	0.13	6				
Wormit Bay	WB5	WB5-6B	MW-IZZI	86	130	3.8	10	6	0.102	0.734	0.762	4.2	3.6%	6.0%	-13.5%	3.5	6.4	1.2	-0.41	3				
Wormit Bay	WB5	WB5-6C	MW-IZZI	101	153	2.8	3	6	0.056	0.481	0.788	8.2	8.0%	10.0%	24.8%	7.5	8.1	4.2	0.11	4				
Wormit Bay	WB5	WB5-H2AI	TH-AF-IZZI	350	560	8.9	20	8	0.161	0.276	0.777	1.6	10.1%	27.3%	-56.4%	12.7	3.0	2.6	0.92	4				
Wormit Bay	WB5	WB5-H3BO	TH-AF-IZZI	450	640	9.3	20	9	0.055	0.416	0.696	7.1	2.6%	4.3%	-6.1%	1.9	1.9	2.4	0.31	6				
Wormit Bay	WB5	WB5-H4-C	TH-AF-IZZI	300	470	21.2	20	5	0.216	0.259	0.628	0.8	10.1%	24.3%	-31.5%	8.0	6.3	4.4	-0.94	2				

Dataset S2:

Sample details			Paleointensity component				Selection criteria													Site mean results			
Site	Sample	Method	Low T (°C)/W.s	High T (°C)/W.s	Pi (μT)	H_{lab} (μT)	n	β	FRAC	g	q	δCK	DRAT	CDRAT	α	MAD_{ANC}	γ	$\vec{k'}$	npTRM	N	Mean Pi (μT)	s.d. (μT)	s.d./ Mean Pi
KH2	KH2-2J	TH-AF-IZZI	400	580	6.5	20	8	0.316	0.310	0.758	0.5	7.0%	33.0%	51.3%	44.0	5.4	7.1	1.15	5				
KH2	KH2-1A	MW-IZZI	17	150	4.0	10	7	0.047	0.399	0.681	9.5	5.7%	8.1%	6.5%	3.8	7.6	10.3	0.33	3				
KH2	KH2-1B	MW-IZZI	18	126	0.9	10	7	0.329	0.400	0.250	0.1	0.9%	9.5%	5.6%	78.8	14.3	10.5	1.59	3				
KH2	KH2-1C	MW-IZZI	88	162	1.7	20	5	0.055	0.434	0.650	8.8	12.5%	16.9%	29.3%	11.8	21.0	2.5	-0.05	5				
KH2	KH2-1D	MW-IZZI	44	135	3.9	10	5	0.021	0.641	0.645	25.6	1.3%	1.4%	1.6%	2.9	6.5	4.9	0.03	3				
KH2	KH2-UA	MW-IZZI	46	133	3.7	10	5	0.095	0.308	0.629	3.6	7.3%	12.7%	12.7%	16.7	6.3	2.5	0.36	3				
KH2	KH2-UZ	MW-IZZI	22	170	2.9	10	8	0.098	0.788	0.719	5.1	13.4%	18.5%	23.2%	12.5	9.0	7.4	-0.34	4				
KH2	KH2-UY	MW-IZZI	0	143	1.5	10	6	0.108	0.526	0.683	4.9	2.4%	3.1%	3.3%	16.3	12.4	4.5	-0.55	2				
KH2	KH2H1A	MW-IZZI	94	119	2.8	10	4	0.339	0.479	0.589	0.9	7.3%	13.9%	19.1%	11.7	20.1	9.6	1.60	3				
KH2	KH2-H2A	TH-AF-IZZI	300	470	7.3	20	5	0.513	0.181	0.716	0.4	15.9%	46.6%	-32.3%	66.9	31.1	6.6	3.16	2	6	6.6	3.0	45%
KH2	KH2-H2B	TH-AF-IZZI	350	580	11.8	20	9	0.160	0.368	0.491	1.3	9.8%	20.7%	36.3%	21.3	3.6	4.5	0.91	5				
KH2	KH2H2A	MW-IZZI	62	109	5.0	10	4	0.038	0.492	0.430	7.1	7.1%	10.0%	8.4%	6.2	3.0	1.9	-0.29	3				
KH2	KH2H2C	MW-IZZI	83	141	6.7	5	7	0.012	0.536	0.794	45.2	11.8%	10.6%	15.0%	3.8	2.6	1.6	-0.05	4				
KH2	KH2H2D	MW-IZZI	80	124	0.8	5	3	0.078	0.189	0.456	1.3	0.6%	2.6%	1.7%	60.0	12.5	7.9	0.18	2				
KH2	KH2L2C	MW-IZZI	22	166	6.4	10	8	0.097	0.220	0.747	4.7	10.8%	14.7%	21.0%	4.9	2.4	4.9	-0.64	4				
KH2	KH2L2D	MW-IZZI	65	164	8.2	10	6	0.065	0.518	0.682	7.9	23.8%	24.5%	33.2%	4.3	3.4	4.2	0.08	4				
KH2	KH2L2E	MW-IZZI	62	147	10.0	5	5	0.080	0.401	0.678	4.2	3.4%	3.1%	0.1%	0.9	1.8	1.3	0.05	3				
KH2	KH2L2F	MW-IZZI	86	211	6.2	10	5	0.084	0.506	0.711	6.8	8.9%	9.5%	14.4%	5.8	5.2	5.8	0.30	4				
KH2	KH2L2G	MW-IZZI	40	181	6.2	5	6	0.051	0.620	0.723	13.1	21.2%	14.5%	17.6%	6.0	5.5	2.7	0.05	4				
KH2	KH2-H4.1	TH-AF-IZZI	0	470	10.6	20	6	0.083	0.416	0.738	6.0	7.7%	10.0%	8.2%	13.8	6.7	6.6	0.43	5				
KH1	KH1-4T	TH-AF-IZZI	500	600	1.3	20	6	0.327	0.354	0.355	0.9	17.9%	22.3%	17.9%	73.0	27.4	7.5	1.54	5				
KH1	KH1-1.5F	TH-AF-IZZI	470	600	3.2	20	7	0.282	0.449	0.457	1.1	12.9%	19.4%	11.8%	7.4	8.8	8.2	1.59	4				
KH1	KH1-U.1B	TH-AF-IZZI	400	580	7.1	20	8	0.092	0.664	0.678	5.5	19.2%	24.4%	24.1%	31.1	15.4	7.1	0.29	5				
KH1	KH1-U.1D	TH-AF-IZZI	400	560	8.3	20	7	0.145	0.484	0.593	1.9	5.4%	10.5%	9.2%	46.6	10.9	9.3	0.71	4				
KH1	KH1-U.1C	TH-AF-IZZI	500	580	3.1	20	5	0.135	0.441	0.615	3.0	32.9%	49.3%	43.0%	18.0	10.5	5.3	-0.48	5				
KH1	KH1-U.1E	TH-AF-IZZI	520	580	2.4	20	4	0.058	0.340	0.541	4.8	30.1%	58.7%	57.6%	27.5	10.3	4	-0.20	5				
KH1	KH1-1A	MW-IZZI	62	156	4.6	10	6	0.057	0.467	0.702	10.3	23.4%	25.5%	21.3%	4.1	5.3	1.2	0.26	4				
KH1	KH1-1B	MW-IZZI	80	153	8.6	10	5	0.135	0.429	0.632	3.3	17.4%	18.6%	9.8%	7.8	6.3	2	-0.65	4				
KH1	KH1-1C	MW-IZZI	62	156	6.4	10	6	0.105	0.378	0.728	4.6	14.0%	17.5%	18.5%	4.2	3.3	1.4	0.32	4				
KH1	KH1-1D	MW-IZZI	45	199	6.9	10	7	0.119	0.639	0.787	6.0	9.8%	8.8%	10.5%	5.1	4.7	2.3	0.61	4				
KH1	KH1-1E	MW-IZZI	61	212	5.5	10	6	0.070	0.628	0.577	7.4	29.3%	28.5%	29.8%	1.5	5.3	3.2	0.40	4				
KH1	KH1-1F	MW-IZZI	42	121	6.7	10	5	0.103	0.650	0.651	5.4	15.2%	14.7%	12.3%	4.5	4.0	2.1	0.54	3				
KH1	KH1-UJ	MW-IZZI	44	163	6.9	5	7	0.049	0.779	0.655	12.5	8.5%	5.3%	-11.9%	2.3	3.9	7.2	0.02	4				
KH1	KH1-UK	MW-IZZI	44	135	5.9	5	6	0.045	0.700	0.754	15.7	12.9%	9.0%	5.2%	3.3	4.0	3.5	0.12	3	12	6.1	1.6	26%
KH1	KH1-UN	MW-IZZI	21	101	3.4	5	5	0.094	0.758	0.653	6.7	1.3%	1.1%	0.3%	2.5	2.6	6.1	0.36	2				
KH1	KH1-UO	MW-IZZI	42	147	5.1	10	7	0.028	0.609	0.715	22.8	0.9%	0.9%	-1.4%	3.9	6.2	7.6	-0.08	4				
KH1	KH1-UP	MW-IZZI	35	133	6.6	5	7	0.071	0.762	0.724	9.5	20.1%	12.9%	8.0%	2.5	2.8	8.7	-0.11	4				
KH1	KH1-UQ	MW-IZZI	68	135	5.0	10	5	0.050	0.677	0.706	12.3	12.9%	13.3%	-9.6%	5.3	4.6	3.9	-0.09	4				
KH1	KH1-H1T	TH-AF-IZZI	540	600	3.6	20	4	0.143	0.366	0.588	3.2	16.3%	20.8%	13.2%	1.6	3.5	11.8	-0.52	5				
KH1	KH1H1A	MW-IZZI	74	152	4.0	5	8	0.062	0.515	0.816	12.2	6.7%	5.6%	-8.8%	3.4	4.9	5.5	0.31	6				
KH1	KH1H1B	MW-IZZI	60	137	7.0	5	9	0.075	0.354	0.811	10.5	16.4%	9.8%	-11.4%	1.8	3.8	1.5	0.45	6				
KH1	KH1H1C	MW-IZZI	84	127	4.8	5	5	0.062	0.327	0.688	8.4	22.4%	21.3%	21.5%	5.1	3.8	1.6	-0.21	5				
KH1	KH1H1D	MW-IZZI	74	101	16.6	5	5	0.140	0.292	0.717	3.3	25.0%	11.1%	-19.2%	5.1	2.3	5.2	0.72	4				
KH1	KH1-H2L	TH-AF-IZZI	440	600	6.4	20	8	0.097	0.524	0.648	3.8	8.7%	14.6%	11.6%	15.0	6.8	2.3	0.41	4				
KH1	KH1H2A	MW-IZZI	96	154	6.2	5	8	0.054	0.389	0.805	8.4	3.2%	3.6%	2.8%	5.8	3.4	4.9	0.21	6				
KH1	KH1H2B	MW-IZZI	67	116	6.1	5	6	0.076	0.492	0.796	7.8	12.3%	10.5%	15.8%	2.9	5.2	7.2	0.24	4				
KH1	KH1H2C	MW-IZZI	66	128	7.1	5	7	0.092	0.473	0.779	4.8	4.7%	4.8%	-2.3%	7.4	3.1	6.1	0.34	4				
KH1	KH1H2D	MW-IZZI	68	141	9.4	5	9	0.073	0.536	0.763	6.3	3.9%	3.0%	-2.3%	4.3	2.6	7.8	0.28	5				
KHA	KHA-1.3E	TH-AF-IZZI	300	470	3.5	20	5	0.161	0.166	0.430	1.1	2.3%	5.7%	-0.7%	40.1	9.6	9.1	-0.09	2				
KHA	KHA-1A	MW-IZZI	62	138	4.3	10	7	0.063	0.461	0.732	9.1	16.8%	19.8%	7.8%	3.0	1.9	1.8	0.28	5				
KHA	KHA-1B	MW-IZZI	62	132	4.0	10	7	0.076	0.358	0.652	5.7	10.1%	14.2%	-1.9%	5.1	2.3	5	-0.01	5				
KHA	KHA-1C	MW-IZZI	64	141	4.2	10	7	0.083	0.508	0.783	7.3	22.0%	26.1%	21.6%	3.8	5.8	4.5	-0.04	5				
KHA	KHA-1D	MW-IZZI	52	130	4.8	10	7	0.094	0.613	0.538	5.1	40.1%	40.8%	30.1%	1.9	4.8	1.5	0.51	4				
KHA	KHA-1E	MW-IZZI	49	134	5.2	10	8	0.095	0.622	0.544	5.0	42.0%	42.2%	15.7%	1.9	3.5	1.4	-0.26	5				
KHA	KHA-1F	MW-IZZI	66	148	3.2	10	7	0.060	0.474	0.682	10.0	7.4%	8.0%	-5.0%	1.9	3.8	0.8	0.01	5	3	3.7	0.5	13%
KHA	KHA-1G	MW-IZZI	34	67	3.9	10	4	0.096	0.476	0.498	4.5	12.8%	13.8%	11.9%	6.9	6.3	1.5	0.26	2				
KHA	KHA-1H	MW-IZZI	33	81	6.3	10	4	0.098	0.608	0.459	4.5	12.3%	10.9%	9.4%	1.0	2.3	18.9	0.55	2				
KHA	KHA-1Z	MW-IZZI	44	164	4.5	10	7	0.102	0.628	0.684	6.1	38.8%	38.7%	21.6%	1.8	3.3	1.8	-0.09	4				
KHA	KHA-2.1A	TH-AF-IZZI	300	520	4.3	20	7	0.324	0.463	0.633	1.5	2.0%	2.5%	2.7%	4.0	6.1	2.5	1.98	3				
KHA	KHA-2.1G	TH-AF-IZZI	300	470	2.1	20	5	0.332	0.148	-0.157	-0.1	0.5%	1.8%	-1.0%	7.6	2.1	20.5	1.49	2				
KHB	KHB-1.2E	TH-AF-IZZI	350	470	2.9	20	4	0.214	0.211	0.535	1.3	0.6%	1.2%	1.8%	19.8	7.5	62.8	0.79	2				
KHB	KHB-1.3B	TH-AF-IZZI	300	560	5.5	20	9	0.196	0.698	0.710	2.6	10.8%	14.5%	-13.5%	31.9	15.5	3	1.11	4				
KHB	KHB-1.3C	TH-AF-IZZI	350	470	1.3	20	4	0.379	0.152	0.511	0.7	0.8%	1.5%	0.8%	5.1	2.6	45.4	1.56	2				
KHB	KHB-1A	MW-IZZI	53	129	6.9	10	7	0.133	0.541	0.685	4.3	37.5%	37.4%	36.2%	4.7	3.9	1.8	-0.37	4				
KHB	KHB-1B	MW-IZZI	50	115	5.1	10	6	0.087	0.650	0.759	6.9	10.7%	12.0%	14.8%	8.7	8.4	2.6	-0.03	4				
KHB	KHB-1C	MW-IZZI	0	137	8.3	10	11	0.079	0.994	0.800	10.6	19.6%	14.5%	7.1%	4.0	10.2	1.1	0.40	5				
KHB	KHB-1D	MW-IZZI	35	82	5.5	10	4	0.142	0.623	0.577	3.5	1.3%	1.3%	-2.7%	9.3	6.5	2.8	0.57	2				
KHB	KHB-1E	MW-IZZI	50	104	5.0	10	5	0.115	0.549	0.625	2.8	0.5%	0.8%	0.4%	32.2	11.4	2.3	0.54	3				
KHB	KHB-1F	MW-IZZI	50	132	6.5	10	8	0.074	0.302	0.780	6.5	10.7%	14.6%	25.1%	7.3	3.5	3.6	0.06	3				
KHB	KHB-1G	MW-IZZI	34	103	5.1	10	6	0.081	0.374	0.679	6.4	2.6%	3.1%	4.0%	2.7	7.1	6.4	0.09	3				
KHB	KHB-1Z	MW-IZZI	65	132	6.7	10	6	0.070	0.548	0.769	8.6	3.1%	3.3%	-1.4%	6.1	4.5	0.9	-0.38	4	9	6.7	2.5	38%
KHB	KHB-2V	TH-AF-IZZI	350	520	5.6	20	6	0.097	0.469	0.604	3.5	17.0%	29.6%	-22.4%	39.0	17.1	10.7	0.12	3				
KHB	KHB-2A	MW-IZZI	60	121	6.3	10	7	0.116	0.602	0.658	4.2	1.7%	1.9%	1.9%	5.9	4.6	6.1	0.60	4				
KHB	KHB-2B	MW-IZZI	55	133	5.4	10	7	0.070	0.508	0.738	7.3	4.3%	5.4%	3.4%	7.0	6.8	6.7	0.25	4				
KHB	KHB-2C	MW-IZZI	53	95	5.9	10	5	0.073	0.623	0.661	6.8	10.1%	11.5%	10.2%	6.7	7.2	5.9	-0.09	3				
KHB	KHB-2D	MW-IZZI	33	83	5.6	10	6	0.087	0.620	0.713	6.0	3.0%	3.6%	2.5%	14.3	10.5	4.3	0.07	3				
KHB	KHB-2E	MW-IZZI	43	88	5.1	10	6	0.071	0.553	0.751	8.8	6.3%	6.7%	4.3%	0.2	4.0	7.8	-0.19	4				
KHB	KHB-3A	TH-AF-IZZI	300	560	8.0	20	9	0.211	0.635	0.704	2.1	9.4%	13.6%	-13.7%	12.4	5.9	4.9	1.25	4				
KHB	KHB-3B	TH-AF-IZZI	400	600	6.0	20	9	0.164	0.557	0.733	3.3	13.5%	17.4%	13.4%	5.4	4.6	3.2	0.56	5				
KHB	KHB-4A	TH-AF-IZZI	350	470	2.8	20	4	0.031	0.239	0.589	8.6	8.4%	18.2%	-21.1%	78.1	24.5	15.3	-0.04	2				
KHB	KHB-4B	TH-AF-IZZI	350	540	12.8	20	7	0.097	0.557	0.698	5.2	6.8%	7.9%	-1.5%	12.5	9.6	5.3	0.04	4				
KH10	KH10-1AI	TH-AF-IZZI	300	520	5.5	20	7	0.201	0.338	0.701	2.7	6.8%	8.4%	12.3%	5.6	4.9	3.5	0.44	3				
KH10	KH10-2BI	TH-AF-IZZI	300	500	6.6	20	6	0.222	0.273	0.634	1.4	7.2%	13.5%	10.9%	8.9	4.4	7	-1.07	3				
KH10	KH10-2A	MW-IZZI	54	150	6.7	5	11	0.078	0.380	0.845	8.5	13.7%	10.4%	-4.6%	13.3	8.8	1.9	0.40	7				
KH10	KH10-3BI	TH-AF-IZZI	300	470	5.4	20	5	0.165	0.356	0.495	1.5	9.3%	18.1%	16.4%	23.3	10.4	6.1	-1.07	2				
KH10	KH10-3A	MW-IZZI	63	107	7.0	5	7	0.092	0.282	0.788	5.9	14.7%	12.3%	4.9%	4.9	3.2	8.8	0.62	2				
KH10	KH10-4BI	TH-AF-IZZI	300	470	4.4	20	5	0.218	0.322	0.417	0.9	10.2%	21.5%	22.0%	22.0	10.7	4.1	2.10	2				
KH10	KH10-5BI	TH-AF-IZZI	300	400	4.0	20	3	0.209	0.204	0.462	0.7	0.2%	0.5%	-0.5%	7.2	4.7	0.9	0.60	1				
KH10	KH10-5A	MW-IZZI	22	76	4.0	5	4	0.069	0.285	0.658	2.9	1.1%	2.9%	2.3%	42.0	8.0	9	0.05	4				
KH10	KH10-6BI	TH-AF-IZZI	300	400	4.2	20	3	0.155	0.188	0.475	1.0	0.1%	0.2%	-0.2%	8.2	5.1	5.3	0.44	1	4	5.2	1.1	22%
KH10	KH10-7AI	TH-AF-IZZI	300	400	4.0	20	3	0.197	0.167	0.423	0.8	0.2%	0.6%	0.6%	11.1	4.0	0.7	0.70	1				
KH10	KH10-8BI	TH-AF-IZZI	300	400	5.6	20	3	0.043	0.341	0.304	4.7	0.1%	0.1%	-0.1%	173.5	6.7	5.2	-0.22	1				
KH10	KH108A	MW-IZZI	43	97	4.0	5	10	0.080	0.595	0.847	9.7	6.8%	5.9%	12.8%	6.4	9.2	3	0.45	4				
KH10	KH108B	MW-IZZI	62	89	3.3	3	7	0.096	0.400	0.804	6.6	12.2%	10.4%	15.0%	9.1	7.2	5	0.53	4				
KH10	KH10-9CI	TH-AF-IZZI	300	400	5.0	20	3	0.005	0.254	0.290	36.1	0.3%	0.5%	0.5%	6.2	4.9	1.8	-0.03	1				
KH10	KH109A	MW-IZZI	65	117	4.9	5	6	0.076	0.365	0.638	5.4	10.0%	11.2%	0.7%	4.3	3.2	2.6	-0.31	4				
KH10	KH109B	MW-IZZI	52	110	5.2	5	9	0.076	0.382	0.819	7.4	6.4%	6.5%	-1.4%	5.7	3.8	9	0.34	5				
KH10	KH109C	MW-IZZI	64	109	5.2	5	7	0.058	0.328	0.803	9.0	12.0%	12.8%	17.9%	7.5	4.6	6.2	0.17	4				
KH4	KH4-3CI	TH-AF-IZZI	450	600	5.0	20	8	0.099	0.568	0.755	6.8	3.8%	4.1%	1.1%	4.4	6.5	2.7	0.42	7				
KH4	KH4-3A	MW-IZZI	107	150	4.8	5	6	0.046	0.357	0.762	5.6	0.6%	1.2%	1.1%	10.8	2.8	3.5	-0.26	3				
KH4	KH4-3B	MW-IZZI	99	152	6.4	5	8	0.025	0.697	0.814	21.6	6.8%	6.2%	12.5%	3.0	1.5	3.5	-0.12	4				
KH4	KH4-4CI	TH-AF-IZZI	450	600	4.8	20	8	0.094	0.653	0.749	7.2	6.2%	6.7%	6.1%	4.2	7.2	3.1	0.41	7				
KH4	KH4-4A	MW-IZZI	0	43	41.0	5	4	0.074	0.292	0.585	2.1	9.8%	4.4%	-4.4%	60.0	12.3	44.6	0.07	1				
KH4	KH4-4B	MW-IZZI	86	142	5.8	5	8	0.052	0.618	0.747	11.1	7.6%	6.4%	-5.9%	4.9	3.9	1.2	-0.15	6	6	5.3	0.7	13%
KH4	KH4-4C	MW-IZZI	89	126	4.8	5	6	0.021	0.452	0.752	16.2	2.7%	4.3%	4.1%	1.3	0.7	1.6	0.08	3				
KH4	KH4-5CI	TH-AF-IZZI	450	570	2.3	20	6	0.152	0.562	0.691	3.7	7.4%	9.0%	9.4%	10.9	13.5	1.1	0.15	6				
KH4	KH4-6BI	TH-AF-IZZI	450	600	4.0	20	8	0.108	0.558	0.767	6.4	4.6%	4.9%	5.4%	6.7	10.1	2.6	0.43	7				
KH4	KH4-8BI	TH-AF-IZZI	300	520	18.7	20	6	0.243	0.588	0.742	2.3	7.2%	6.8%	-16.3%	8.9	5.1	3.6	0.69	3				
KH7	KH7-1CI	TH-AF-IZZI	300	500	11.3	20	5	0.260	0.288	0.644	1.2	2.0%	3.6%	-5.4%	9.9	3.4	4.9	1.28	2				
KH7	KH7-2CI	TH-AF-IZZI	300	500	11.7	20	5	0.276	0.273	0.647	1.2	2.2%	3.9%	-6.7%	11.0	3.7	2.3	1.34	2				
KH7	KH7-3CI	TH-AF-IZZI	300	500	21.7	20	5	0.241	0.421	0.661	1.2	4.0%	6.3%	-7.3%	5.2	2.2	2	1.17	2				
KH7	KH7-4CI	TH-AF-IZZI	300	500	18.8	20	5	0.247	0.432	0.641	1.2	6.1%	9.6%	-12.7%	5.2	2.0	1.1	1.30	2				
KH7	KH7-5BI	TH-AF-IZZI	450	600	10.5	20	8	0.066	0.486	0.850	9.9	5.5%	6.3%	-23.3%	3.3	4.5	3.8	0.19	7				
KH7	KH7-5A	MW-IZZI	80	125	15.4	5	8	0.027	0.602	0.834	20.1	8.4%	4.1%	-11.8%	3.0	1.3	3	0.14	5				
KH7	KH7-5B	MW-IZZI	75	199	13.8	5	13	0.016	0.780	0.877	43.4	8.1%	3.5%	-8.5%	3.2	2.4	3.6	-0.03	7	4	10.9	4.3	40%
KH7	KH7-6BI	TH-AF-IZZI	300	500	19.9	20	5	0.287	0.382	0.639	0.8	2.0%	3.8%	-4.4%	4.7	2.3	2.8	1.54	2				
KH7	KH7-7CI	TH-AF-IZZI	300	500	22.4	20	5	0.275	0.385	0.652	0.9	3.9%	6.8%	-10.8%	5.7	1.6	2.3	1.40	2				
KH7	KH7-8CI	TH-AF-IZZI	500	620	6.7	20	8	0.074	0.363	0.811	7.3	6.6%	9.4%	9.6%	4.5	4.8	1.5	0.36	7				
KH7	KH7-8A	MW-IZZI	96	141	7.7	5	7	0.047	0.404	0.809	9.5	6.2%	6.1%	8.6%	2.2	1.7	3.4	0.38	5				
KH7	KH7-8B	MW-IZZI	79	114	10.0	20	6	0.044	0.328	0.749	6.7	6.2%	13.8%	14.1%	5.1	1.8	1.4	1.56	5				
KH8/9	KH8-1BI	TH-AF-IZZI	400	580	3.3	20	8	0.111	0.578	0.824	6.8	8.2%	8.9%	18.9%	9.7	10.2	1.3	0.59	7				
KH8/9	KH8-1A	MW-IZZI	66	99	5.3	5	6	0.083	0.466	0.714	4.7	3.2%	3.9%	2.6%	8.3	2.4	6.3	0.40	3				
KH8/9	KH8-1B	MW-IZZI	73	103	4.4	5	6	0.030	0.465	0.770	15.3	6.8%	8.5%	11.9%	9.7	4.4	5.2	0.09	4				
KH8/9	KH8-2BI	TH-AF-IZZI	400	580	2.5	20	8	0.140	0.472	0.830	4.5	7.5%	9.9%	21.8%	10.7	9.9	3.3	0.56	7				
KH8/9	KH8-3BI	TH-AF-IZZI	400	600	4.2	20	9	0.091	0.492	0.860	8.9	12.4%	12.8%	27.9%	1.5	2.5	2.1	0.26	7				
KH8/9	KH8-4BI	TH-AF-IZZI	450	600	3.6	20	8	0.103	0.533	0.843	6.8	13.4%	15.8%	29.6%	2.1	3.3	4.2	-0.15	7				
KH8/9	KH8-H1CI	TH-AF-IZZI	500	620	6.7	20	7	0.131	0.437	0.761	4.7	9.0%	10.5%	16.4%	0.7	1.1	1.8	0.69	6				
KH8/9	KH8H1A	MW-IZZI	77	188	12.7	5	11	0.028	0.705	0.875	26.3	10.7%	4.7%	8.3%	1.4	1.1	1.2	-0.10	7				
KH8/9	KH8-H2AI	TH-AF-IZZI	400	540	7.8	20	6	0.128	0.435	0.705	2.9	17.0%	30.1%	40.2%	10.2	2.8	2.2	0.00	4				
KH8/9	KH9-1BII	TH-AF-IZZI	500	580	1.8	20	5	0.065	0.397	0.710	5.6	16.6%	32.3%	40.1%	3.5	14.1	2.7	-0.28	5				
KH8/9	KH9-1A	MW-IZZI	63	132	4.9	5	8	0.057	0.803	0.848	12.9	20.2%	16.6%	36.7%	3.1	3.5	2.1	0.24	5				
KH8/9	KH9-1B	MW-IZZI	74	116	5.1	5	6	0.042	0.466	0.760	9.8	7.9%	10.3%	15.1%	5.9	2.1	8.4	-0.05	3	9	8.6	4.0	47%
KH8/9	KH9-2BII	TH-AF-IZZI	300	500	22.2	20	6	0.210	0.398	0.755	1.8	7.2%	9.8%	5.1%	13.5	3.9	4.6	0.62	3				
KH8/9	KH9-3AII	TH-AF-IZZI	300	500	27.6	20	6	0.173	0.432	0.749	2.1	4.7%	5.7%	0.0%	11.3	3.3	3.2	0.66	3				
KH8/9	KH9-3A	MW-IZZI	45	96	5.0	5	4	0.019	0.584	0.495	18.3	2.4%	2.4%	2.8%	2.4	3.8	2.7	-0.11	2				
KH8/9	KH9-3B	MW-IZZI	44	122	6.3	5	9	0.035	0.719	0.826	18.4	10.5%	8.3%	14.5%	2.9	2.0	3.6	-0.01	5				
KH8/9	KH9-3C	MW-IZZI	44	110	5.2	5	7	0.022	0.400	0.774	15.4	3.6%	5.8%	7.3%	10.0	2.3	4.2	0.08	3				
KH8/9	KH9-4AII	TH-AF-IZZI	300	500	46.7	20	6	0.161	0.536	0.753	2.3	14.6%	11.5%	16.1%	5.9	1.8	7.7	0.57	3				
KH8/9	KH9-4A	MW-IZZI	60	110	13.1	5	7	0.071	0.732	0.817	8.9	13.0%	6.0%	4.0%	1.1	0.8	0.3	0.24	4				
KH8/9	KH9-4B	MW-IZZI	67	120	13.5	5	10	0.033	0.823	0.830	20.3	5.2%	2.3%	-2.6%	2.1	1.5	0.9	0.12	5				
KH8/9	KH9-4C	MW-IZZI	72	137	12.0	10	10	0.018	0.645	0.876	30.3	6.0%	6.1%	10.5%	1.7	0.8	1.3	0.14	5				
KH8/9	KH9-5BII	TH-AF-IZZI	300	500	19.4	20	6	0.194	0.317	0.730	1.7	7.3%	11.3%	14.9%	12.3	2.9	2	0.57	3				
KH8/9	KH9-5A	MW-IZZI	88	107	4.2	5	3	0.345	0.465	0.431	0.5	0.6%	1.0%	1.0%	8.3	5.9	2.1	1.58	1				